UNIVERSITY OF OKLAHOMA

GRADUATE COLLEGE

BLOOD DAMAGE ANALYSIS USING COMPUTATIONAL FLUID DYNAMICS OF BLOOD FLOW THROUGH A FUNCTIONING AND MALFUNCTIONING BILEAFLET ARTIFICIAL HEART VALVE

A THESIS

SUBMITTED TO THE GRADUATE FACULTY

in partial fulfillment of the requirements for the

Degree of

MASTER OF SCIENCE

By

MADISON JAMES
Norman, Oklahoma
2018

BLOOD DAMAGE ANALYSIS USING COMPUTATIONAL FLUID DYNAMICS OF BLOOD FLOW THROUGH A FUNCTIONING AND MALFUNCTIONING BILEAFLET ARTIFICIAL HEART VALVE

A THESIS APPROVED FOR THE
STEPHENSON SCHOOL OF BIOMEDICAL ENGINEERING

BY

_____
Dr. Edgar A. O'Rear, Co-Chair

_____
Dr. Dimitrios V. Papavassiliou, Co-Chair

_____
Dr. Matthias U. Nollert

I dedicate this thesis to my family who has always supported me and stressed the importance of creativity, discovery and hard work.

Acknowledgements

I would like to thank my advisors Dr. Edgar O'Rear and Dr. Dimitrios Papavassiliou for their continued support, advisement, and encouragement throughout the entire process. I appreciate all of the time taken to meet with me and offer guidance for my project.

I also would like to thank Dr. Matthias Nollert for being one of my thesis committee members.

I am deeply appreciative of the University of Oklahoma Department of Chemical, Biological and Materials Engineering (CBME) for awarding me funding through the Program of Excellence Research Scholarship.

I am very thankful for the help and guidance provided by Mesude Ozturk in how to use ANSYS software and how to do the calculations. I also appreciate the consistent and helpful support provided by Horst Severini, Kali McLennon, Henry Neeman, and all others involved the University of Oklahoma Supercomputing Center for Education & Research (OSCER).

Finally, I would like to thank all of my family and friends for their support, encouragement, and understanding through this process.

Table of Contents

List of Tables

List of Figures

Abstract

Artificial heart valves are an invaluable tool to treat heart defects and diseases. However, these prosthetic devices may expose the blood to turbulent flow conditions leading to unnaturally high stress that can damage blood cells.

The purpose of this research is to simulate blood flow in both a functioning and malfunctioning bi-leaflet artificial heart valve and predict the damage caused to red blood cells (RBCs), specifically hemolysis, from the magnitude of the stress and exposure time as determined by analysis of the turbulent flow eddies. Using the computational fluid dynamics (CFD) software ANSYS DesignModeler, two prosthetic heart valve models were constructed: one with both leaflets open and functioning and one with one leaflet mostly closed. Blood flow simulations were done using ANSYS Fluent and validated with experimental findings available in the literature. Results from the CFD simulations provided the spatial distribution of Kolmogorov length scales (KLS) that were used to find the spatial and size distributions of eddies in the flow field. This CFD-based research utilized the number and surface area of eddies in the blood as a way to predict the amount of hemolysis experienced by RBCs. The analysis is centered on the hypothesis that only some of the turbulent flow eddies – those with sizes comparable to or smaller than the size of RBCs – are the ones that contribute to cell damage.

Results indicated that hemolysis levels are low, suggesting the need for further study of subhemolytic damage. The hemolysis predictions did allow for a comparative analysis of the heart valve simulations, which showed that more damage is expected at a higher flowrate, and that at the same flowrate, more damage is expected in the malfunctioning valve when compared to the functioning valve.

1 Introduction

Heart disease is the leading cause of death (1 in every 4) in the United States[1]. In 2016, it was estimated that over 28.1 million people are affected by heart diseases and disorders, which is more than 10% of the adult population[2]. Common heart problems include coronary artery disease, often treated with a coronary bypass surgery or angioplasty; congestive heart failure, treated with transplants and ventricular assist devices (VADs); and heart valve diseases, treated with prosthetic heart valves. This research will focus on analyzing the damage caused by these artificial heart valves.

1.1 The Circulatory System

The circulatory system is important for transporting oxygen and nutrients around the body. It is comprised of the heart, blood, and blood vessels. The human heart is divided into four chambers: the left and right atria and the left and right ventricles. Four heart valves separate the chambers from each other and the major arteries: the mitral valve, aortic valve, tricuspid valve, and pulmonary valve (Figure 1.1).

Blood receives oxygen from the lungs and is transported to the heart through the pulmonary vein and into the left atrium. The heart then pumps blood through the mitral valve, into the left ventricle before sending it through the aortic valve, into the aorta, and out to the rest of the body. While moving through the body, the blood receives and delivers nutrients and waste. The deoxygenated blood from the body travels through the vena cava into the right atrium where it is pumped through the tricuspid valve into the right ventricle. Finally the blood travels through the pulmonary valve into the pulmonary artery that carries blood to the lungs to be re-oxygenated.

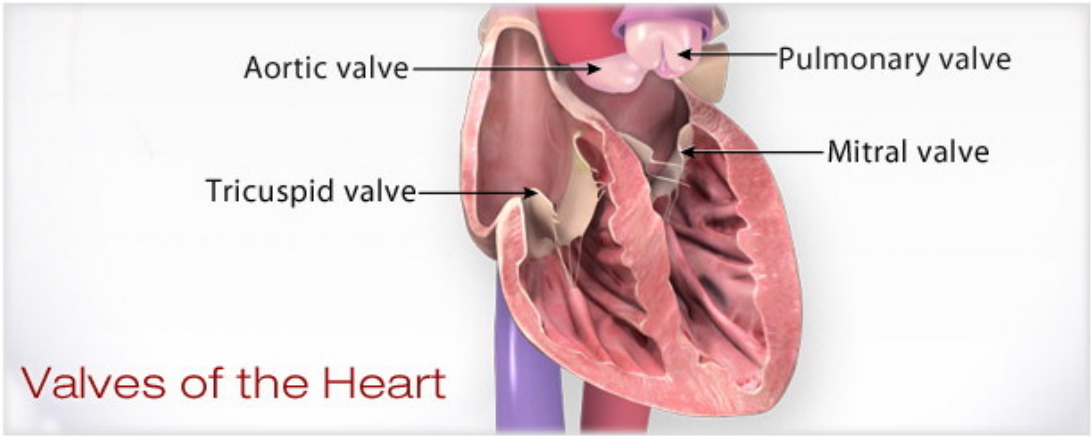

Figure 1.1 Diagram of heart valves[3]

On average, an adult human holds about 5 L of blood, which equates to about 8% of their body weight. Blood is made up of about 55% plasma and 45% blood cells by volume. Plasma is composed of about 90% water, 8 % protein, and 2% inorganic salts and organic material. Blood cells are composed of a ratio of 600 red blood cells (RBCs) to 40 platelets to 1 white blood cell[4].

1.2 Heart Valve Disease and Treatments

1.2.1 Heart Valve Diseases

An initial indication of a heart valve problem is a heart murmur, an unusual noise made by the heart that often sounds like a whoosh or click when a doctor is checking a patient's heartbeat[5]. It is possible that is just an innocuous heart murmur; however, it could also be a symptom of one of many heart valve disorders like stenosis, regurgitation, prolapse, or atresia[6].

Stenosis occurs when a narrowing of the heart valve prevents blood from flowing through, often caused when the valve is too thick or when two of three leaflets in a valve fuse together (Figure 1.2)[7]. This disorder can affect any of the four heart valves. The decrease in the stroke volume decreases the oxygen supply and causes the

heart to work harder. According to the American Heart Association, aortic stenosis is "one of the most common and most serious valve disease problems[8]."

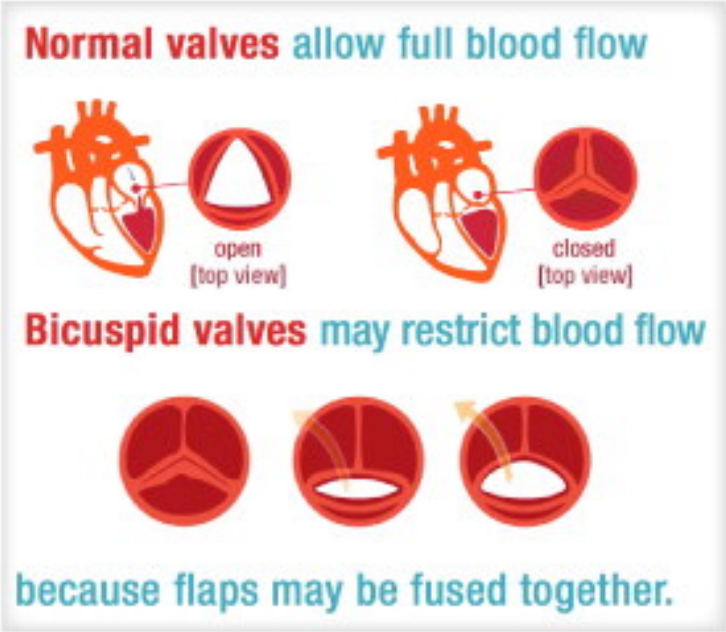

Figure 1.2 Diagram of valve stenosis[8]

Heart valve regurgitation occurs when the heart valve allows blood to flow backwards into the chamber. This leaking usually occurs as the leaflets are closing or when the leaflets fail to seal fully[9]. As with stenosis, regurgitation can affect any of the heart valves. The stroke volume is again lower than it should be, decreasing the oxygen supply and increasing the heart's work load.

As its name suggests, mitral valve prolapse only occurs in the mitral valve. This disorder occurs when the leaflets of the mitral valve do not close properly. They bulge into the chamber and collapse backwards, allowing small amounts of blood to leak into the previous chamber[10].

Atresia is the general name for a disorder in which any of the valves are malformed or completely missing. For example, in pulmonary atresia, the pulmonary

valve is missing, and blood is prevented from flowing into the pulmonary artery and out to the lungs[11]. Or, in tricuspid atresia, the tricuspid valve is missing, and blood is prevented from flowing into the right ventricle[11].

1.2.2 Heart Valve Disease Treatments

Patients with heart valve diseases and defects have two main treatment options: valve repair and valve replacement. In valve repair, the patient is able to keep their own valve and leaflets, though this is most common for only mitral and tricuspid valve regurgitation[12]. The alternative, valve replacement, requires a brand new valve to be surgically inserted into the patient's heart.

Replacement heart valves are classified as either mechanical or bioprosthetic (made of tissue). Common mechanical valves include the bileaflet, tilting disk, and ball-and-cage valves (Figure 1.3). The most common bioprosthetic valves are made from either bovine (cow) or porcine (pig) tissue. Continued research is still being done to improve replacement heart valves and optimize their design. Bioprosthetic valves have a shorter life-span than mechanical valves, but mechanical valves are less biocompatible and more aggressively rejected by the body[13]. Moreover, genetic modification of pigs offers the prospect of reducing rejection of porcine prostheses.

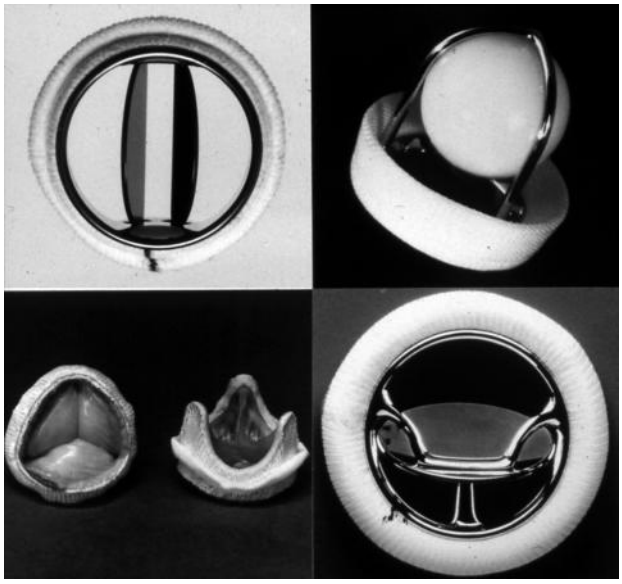

Figure 1.3 Common types of heart valve prostheses: St Jude's Medical bileaflet (top left); Starr-Edwards ball and cage (top right); Bjork-Shiley tilting disc (bottom right); stented porcine prosthesis (bottom left)[14]

1.3 Blood Damage

For both valve types, another major concern is the unnatural flow conditions these foreign objects expose the blood to. The stresses of non-physiological turbulent flow can be damaging to blood cells[15, 16]. Continued research has worked to fully characterize turbulence and the effect it has on blood[17, 18]. Two major concerns are thrombosis, the formation of a blood clot (thrombus), and hemolysis, the release of hemoglobin from red blood cells (RBCs). Erythrocytes can lose hemoglobin by rupture of the cell membrane or the temporary formation of pores in the membrane (Figure 1.4). Hemoglobin, a cytoplasm molecule whose solution makes up 90% of the volume of RBCs, binds to oxygen molecules and allows oxygen to be carried and delivered throughout the body. The red cell also assists in the removal of carbon dioxide from tissues and its transport to the lungs. When hemoglobin is released into the blood

stream it lowers the oxygen carrying capacity of the blood and, in too high of levels, can be toxic to the body.

Figure 1.4 An illustration of a red blood cell undergoing hemolysis[19]

Under the same wall shear stress in a capillary tube, it has been found that turbulent flow causes significantly more hemolysis than laminar flows[18]. Both high laminar (viscous) and high turbulent stresses can be damaging to the blood. Various research groups have investigated the minimum viscous stress threshold in laminar flow and minimum stress threshold in turbulent flow necessary to induce hemolysis[20-25]. However, there is still uncertainty and argument about these threshold limits and even whether Reynolds stresses are appropriate to describe cell damage for turbulent flow.

1.4 Blood Damage Predictions

Blackshear et al. first introduced the dependence of hemolysis on shear stress and exposure time[26]. The power law model (Equation 1.1) is now commonly used to calculate the amount of hemolysis, or hemolysis index (*HI*), expected for a given flow based on shear stress (τ), exposure time (t), and experimental coefficients (α, β, and C).

The hemolysis index is the ratio (as a percent) between the increase in free plasma hemoglobin and the whole blood hemoglobin in a sample of blood.

$$HI = C\tau^{\alpha}t^{\beta} \qquad \textbf{Equation 1.1}$$

This equation showed that either high stress for a short time or low stress for an extended period of time can be damaging. The power law model was first used by Giersiepen et al. to predict hemolysis in artificial heart valves based on data obtained from experiments with a Couette viscometer[27]. Other investigators have continued to use in-vitro experimentation to predict the amount of hemolysis on blood due to shear stresses[24, 28-30]. Additional research has modified this equation, looked at additional variables or information from the blood, or completely changed the approach to create new prediction models[31-36]. For example, Arvand et al. modified the power law model to predict hemolysis from the mean exposure time and comparative shear stress, as well as the volume share (accumulation of all elemental volumes with the critical comparative shear stress) and pressure head[31]. Arora et al. used a tensor based model to describe cell shape and strain to predict hemolysis[34]. Vitale et al. used a three component process to predict hemolysis using deformation of the RBC, permeability of the cell membrane, and hemoglobin transport[35]. However, these predictions have a limited usefulness.

Many of the models have been largely based on data obtained from laminar flow conditions, but blood flow through the heart is known to be turbulent [37, 38]. The shearing stresses in laminar and turbulent flow are inherently different, so it is unlikely that prediction obtained from idealized laminar flow conditions can predict the complexity of the mixing boundary layers and shearing stresses in turbulent flow. The

complexity of turbulent flow also opens the possibility of extensional stresses contributing to hemolysis. Additional research has analyzed hemolysis under turbulent conditions relative to viscous, Reynolds, and total stresses, but have had limited success so far as research has yet to determine which specific stresses or even deformation causes hemolysis[15, 16, 39-41].

Data for the models are also predominantly generated using various Couette viscometers or pump devices. The constant shear stresses of viscometer experiments cannot fully capture the damage expected from turbulent flow. The specifics of these conditions do not allow for a wide-range general use of the equations. This necessitates the use of a device-independent equation that can be used for artificial heart valves as well as ventricular assist devices and pumps. Still, the majority of computational research in this area continues to use the power law model for predictions.

A study analyzing the applicability of viscous and Reynolds stresses conducted flow simulations of turbulence and analyzed hemolysis in a Couette viscometer and capillary tube [42]. This study found that there is no common threshold value for hemolysis for either viscous or Reynolds stresses. This shows that neither stress type seems to be a good predictor of hemolysis. As such, this research aims to use a different approach for predicting hemolysis caused by artificial heart valves by instead focusing on dissipative energy rates and eddies as a possible predictor of hemolysis.

1.4.1 Blood Damage Predictions in Artificial Heart Valves

Hemolysis and decreased RBC survival due to prosthetic heart valves has been reported since the 1960's[43]. Over time the reported percent of patients who experience hemolysis after implantation have decreased, from optimization of valve

types and structure[44-46]. There is still some disagreement about the extent of hemolysis due to artificial heart valves. While clinical studies show a prevalence of subclinical hemolysis (with a low incidence of hemolytic anemia or clinically severe hemolysis) in valve replacement patients[47-49], current in-vitro and CFD research into hemolysis damage are still measuring and predicting damage to RBCs from notable amounts of hemolysis caused by artificial heart valves[50-53]. (Though the actual calculation and prediction of hemolysis remains extremely limited.)

In an in vitro study, Susin et al. used an adapted form of the power law model to predict the hemolysis index from in vitro water flow results[50]. They used a pulse duplicator system with a simplified model of the human ascending aorta and left ventricle outflow tract and a bileaflet Sorin Bicarbon Slimline valve to model the flow[50]. This set up was used to determine an exposure time and shear stress of the fluid, which were plugged into the equation (Table 1.1) to predict the expected hemolysis. The calculated HI ranged from 2.05×10^{-5} to 7.01×10^{-5}% for stroke volumes of 64 and 80 mL and exposure times of 2.4 and 2.6 seconds[50].

Using ANSYS CFD, Tullio et al. modeled flow through a St. Jude mechanical valve with both a standard and Valsalva graft, and compared two stress-based and one strain-based prediction model for hemolysis[51] (Table 1.1). In their model, the group considered blood to be a Newtonian fluid. The predicted hemolysis means and maximums ranged from 1.701×10^{-5} to 366.0×10^{-5}%. In both cases, the units of exposure time (t) is seconds and the units of shear stress (τ) is pascals. The various models and hemolysis predictions are summarized in Table 1.1.

Table 1.1 Hemolysis Models and Predictions for Artificial Heart Valve

	Model	**Hemolysis Prediction (%)**
Susin[50]	$HI = 3.62 * 10^{-5} * t_{exp}^{0.785} * \tau^{2.416}$	2.05 – 7.01 x 10^{-5}
Tullio[51]	$\Delta HI_i = \alpha C t_i^{\alpha-1} \tau(t_i)^{\beta} \Delta t_i$	Max: 149.4 – 157.2 x 10^{-5} Mean: 6.880 – 7.097 x 10^{-5}
Tullio[51]	$\Delta HI_i = C\alpha \left[\sum_{j=1}^{i} \tau(t_j)^{\beta/\alpha} \Delta t_j + HI(t_0)\right]^{\alpha-1} \tau(t_i)^{\beta/\alpha} \Delta t_i$	Max: 352.8 – 366.0 x 10^{-5} Mean: 10.03 – 10.38 x 10^{-5}
Arora[34]	$\frac{\Delta Hb}{Hb} = 3.62x10^{-7}\left(\mu_{blood}\sqrt{\frac{{f_1}^2}{(1-D^2){f_1}^2}}\right)^{2.416} t^{0.785}$	Max: 64.87 – 66.07 x 10^{-5} Mean: 1.701 – 1.756 x 10^{-5}

Many studies have shown a distinct difference in the incidence of hemolysis cases (clinical studies) or the amount of free plasma hemoglobin (in-vitro studies) between different valve types[47, 48, 54]. For example, in a clinical study by Mecozzi et al., there was a distinct difference in the incidence of subclinical hemolysis in patients with stented vs. stentless valves or with different types of prosthetic valves[47]. Linde et al. found in an in-vitro study that there was a statistically significant difference in the free plasma hemoglobin levels between a St Jude mechanical bileaflet valve and a trileaflet valve prototype[54].

The various groups who have modeled and continue to model flow through heart valves attempt to predict hemolysis based on flow conditions using various models, including the Power Law model. However, clinically, hemolysis problems are commonly related to issues other than flow through the valve or valve design. Most

often, incidences of high hemolysis are due to paravalvular leakage rather than damaging flow conditions created by the heart valve itself[55-57]. This research aims to use an alternative prediction model to capture the low levels of hemolysis seen clinically.

1.5 Eddy Analysis

Eddies are spots of localized circulation in the fluid, idealized in the shape of a sphere. Turbulence is complex, so eddies have been used to characterize the microstructure of the flow to be related to the expected damage to RBCs[16, 17, 58-60]. The total surface area of these eddies is of major importance, because damage to cells likely occurs at the interface of eddies by both shear and extensional stresses.
The Kolmogorov length scale (KLS) is the smallest dissipative length scale that can be used in turbulent flow, and is used to represent the diameter of eddies. KLS is calculated (Equation 1.2) from the results of flow modeling using CFD, using v, the kinematic viscosity (ratio of dynamic viscosity over density, $\frac{\mu}{\rho}$), and ϵ, the turbulent dissipation rate.

$$KLS = \left(\frac{v^3}{\epsilon}\right)^{\frac{1}{4}} = \left(\frac{\mu^3}{\rho^3 \epsilon}\right)^{\frac{1}{4}} \qquad \textbf{Equation 1.2}$$

Previous research found that as cumulative eddy area per unit volume increased for a given size eddy, the hemolysis index also increased[61]. However, this relationship only exists for KLS sizes up to 10 μm. Beyond that point, large size eddies did not appear to be related to hemolysis index, which was shown to be true for computational models of a Couette viscometer, capillary tube, and jet (Figure 1.5). This research also showed that when comparing hemolysis of cumulative KLS values, at and

above 12 μm there was little additional eddy area (Figure 1.6)[62]. This means that eddies the size of or smaller than RBCs are the most damaging[61], while those larger than RBCs just shift the cells from their path in the overall bulk flow. Because of these findings, this research focuses on eddies with a diameter of 10 μm or less.

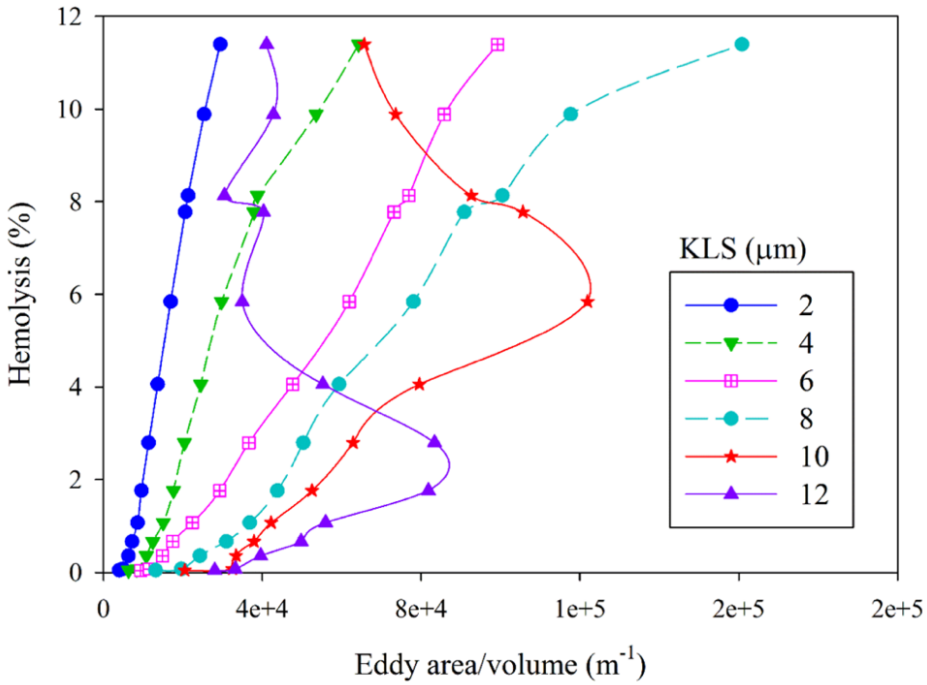

Figure 1.5 Hemolysis as a function of eddy sizes and area/volume in a simulation of Forstrom's jet experiments[62, 63]

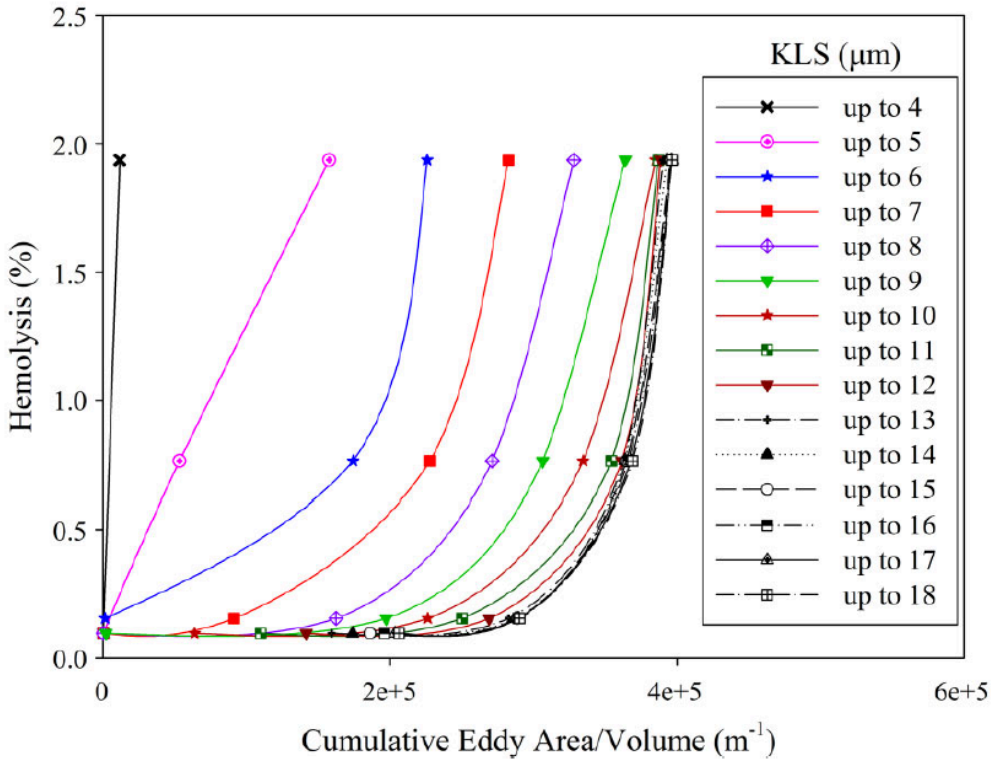

Figure 1.6 Hemolysis as a function of eddy sizes and cumulative area/volume in the capillary tube model[62]

Both eddy intensity and spatial distribution are important considerations. Eddy intensity relates to the local damage. A higher eddy intensity means a greater number of small eddies in a region. A greater number of smaller eddies means more viscous dissipation and more damage to cells. Spatial distribution relates to the likelihood that RBCs encounter a region of high eddy intensity. More regions throughout the flow field means RBCs are more likely to encounter a region and thus more damage to cells. CFD modeling can be used to capture the relative extent of regions likely to cause damage.

Two new equations (Equation 1.3 and Equation 1.4) have been proposed that utilize the surface areas of eddy to predict hemolysis. In these equations, *HI* is the hemolysis index (% hemolysis); *t* is the exposure time in seconds; *a*, *b*, *c*, *d* , and *e* are

experimental coefficients; and $EA_{KLS(D1-D2)}$ is the total eddy surface area of eddies in the size range D1 to D2 divided by the total volume of the region composed of eddies up to 10 μm (in m^{-1})[62]. Equation 1.3 includes surface areas of eddies up to 10 μm in diameter, while Equation 1.4 includes surface areas of eddies up to 9 μm. These equations were developed by modeling three classical hemolysis experiments of turbulent flow: a Couette viscometer, a capillary tube, and a jet[18, 22, 63]. These computational experiments were analyzed by KLS size distribution for 24 conditions and 5 orders of magnitude of exposure time to obtain coefficients in Equations 1.3 and 1.4 (Table 1.2).

$$HI = bt + c * EA_{KLS(0-4)} + d * EA_{KLS(5-7)} + e * EA_{KLS(8-10)} \quad \textbf{Equation 1.3}$$

$$HI = a + bt + c * EA_{KLS(0-3)} + d * EA_{KLS(4-6)} + e * EA_{KLS(7-9)} \quad \textbf{Equation 1.4}$$

Table 1.2 Coefficients for Equations 1.3 and 1.4

	a	**b**	**c**	**d**	**e**
Equation 1.3	—	5.57×10^{-4}	2.45×10^{-5}	2.67×10^{-6}	1.14×10^{-6}
Equation 1.4	1.62×10^{-7}	1.82×10^{-7}	3.08×10^{-5}	3.42×10^{-6}	1.72×10^{-6}

1.6 Objective

This research aims to use computational fluid dynamics to analyze the flow of blood through an artificial heart valve and apply eddy analysis to predict hemolysis. Specifically, this research will compare characteristics of the flow in a functioning and a malfunctioning bileaflet artificial heart valve. Though there have been numerous studies modeling flow of artificial heart valves, there has been a very limited amount of computational research into heart valve leaflet malfunction[64-66]. This work will examine turbulent flow in a fully functioning valve in silico with both leaflets in the

fully open position and a malfunctioning valve with one leaflet in the fully open position and one leaflet in a mostly closed position.

Additionally, this research aims to employ the CFD results to analyze the distribution and intensity of eddies with a KLS of 10 μm or less for both valves at different flowrates. As an alternative to the commonly used power law model, the hemolysis predictions of a functioning and malfunctioning bileaflet valve will be calculated using KLS results and eddy surface areas. Predictions from these two equations will be compared across both valve representations at different flowrates.

2 Methods

Computational fluid dynamics (CFD) allows for the modeling of a fluid system and the numerical calculations and predictions of various characteristics of that flow. CFD requires the virtual creation of a geometry, the meshing of that geometry, setting solution parameters for equations, specifically flow conditions, and post processing the results. All of the CFD work in this research was done using ANSYS software.

2.1 Geometry Model

A bileaflet heart valve was modeled because bileaflet heart valves are not only the most commonly implanted mechanical heart valve, but also the most commonly implanted mechanical prosthetic[14, 67]. Valve structure was created based on an experimental system used by Hutchinson[68]. This specific model was selected because of the detailed schematics available, which would allow for a more accurate computational representation for comparison, and the imagining method chosen for experimental measurements. An example of the schematics used is shown in Figure 2.1. Additional schematics used are shown in the Appendix. This group used Particle Imaging Velocimetry (PIV), one of the most commonly used imaging techniques, which has been found to have a greater resolution than other imaging methods like magnetic resonance imaging (MRI) and Doppler[67]. His experimental system was created based on the Carbomedics No. 25 aortic bileaflet mechanical heart valve (Figure 2.2).

All of the dimensions used in the CFD model were taken from the various schematics included in Hutchinson's work[68]. The Hutchinson experimental system consists of a 400 mm inlet with a 26.8 mm diameter, that leads to a 7.7 mm long valve

frame (Figure 2.1). The valve channel has a radius of 10.25 mm, but two sides are flat with parallel chords, at a slightly shorter distance of 9.075 mm from the center. Inside the valve are two leaflets with straight edges 18.15 mm wide at the entrance to the valve and curved edges at the outlet. The leaflets have a maximum length of 11.31 mm from edge to edge and are .76 mm thick. In the functioning valve model used by Hutchinson both leaflets are at a 78° angle. In the malfunctioning model, one of the leaflets is tilted 65° back towards the closed position to model a mostly closed leaflet. The valve leads into a sinus with a 32 mm diameter, that gradually decreases to 26.8 mm and continues into a 270 mm long outlet. The variation in sinus diameter, as reported by Hutchinson[68], is given in Table 2.1. A diagram of the entire model is shown in Figure 2.3.

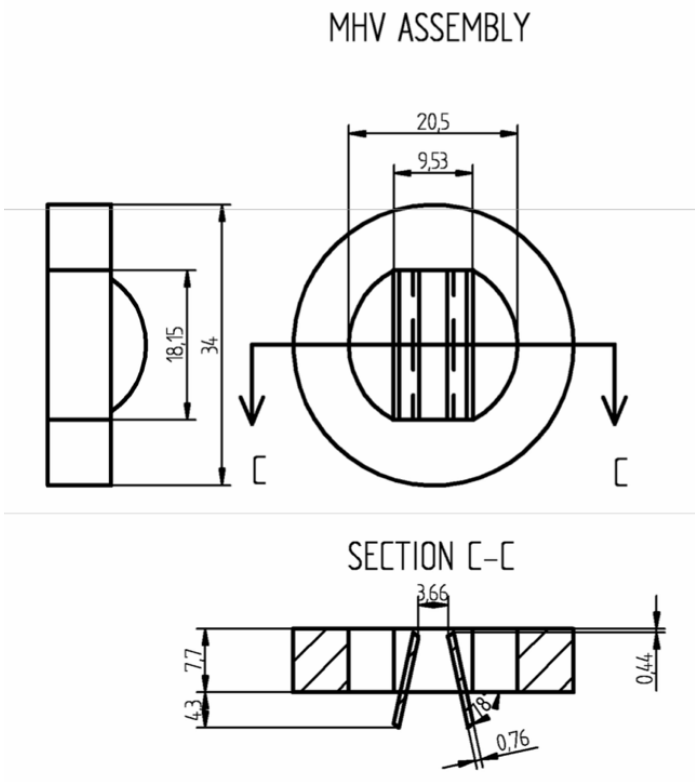

Figure 2.1 Schematic of valve model used by Hutchinson[68]

Figure 2.2 Carbomedics artificial aortic heart valve[69]

Table 2.1 Radius along the length of the aortic sinus[68]

x (mm)	radius (mm)
407.7	16.00
425.8	16.00
426.8	15.96
427.8	15.94
428.8	15.92
429.8	15.88
430.8	15.81
431.8	15.66
432.8	15.38
433.8	14.89
434.8	13.54
435.5	13.40

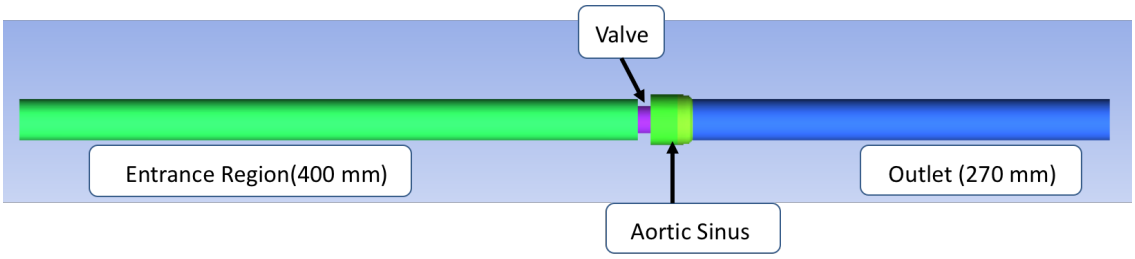

Figure 2.3 Diagram of the entire heart valve model

The heart valve models were created using ANSYS DesignModeler 18.1 in Workbench. Both designs were three dimensional to represent characteristics of the flow better. The functioning heart valve is symmetric across both the horizontal and vertical planes, so only a quarter of the valve was modeled (Figure 2.4). The malfunctioning heart valve is symmetric across the vertical plane bisecting the leaflets, so only half of the valve was modeled (Figure 2.5). ANSYS software allows for the creation of symmetric planes, which decreases the amount of mesh cells needed and computation time required.

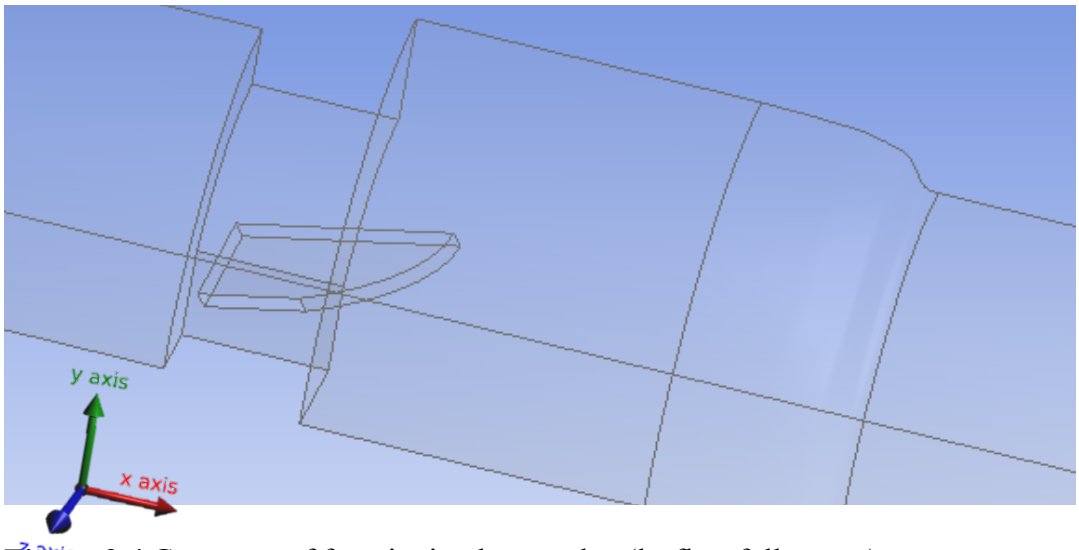

Figure 2.4 Geometry of functioning heart valve (leaflets fully open)

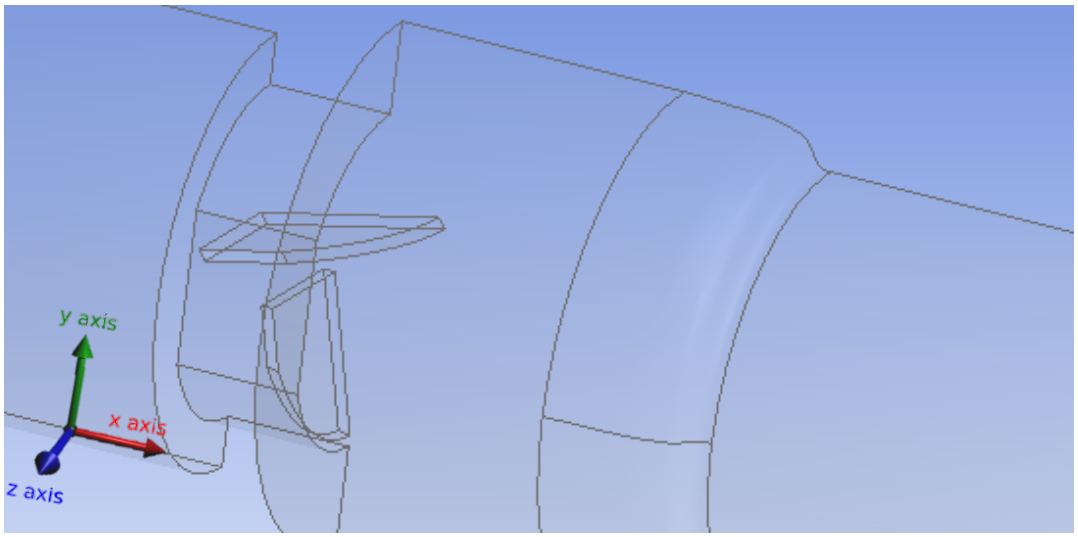

Figure 2.5 Geometry of malfunctioning heart valve (one leaflet mostly closed)

2.2 Meshing

The meshing was done using Mesh in ANSYS Workbench 18.1. A medium tetrahedral mesh was automatically created for both domains. The mesh included an inflation layer, which is a set of hexahedral cells surrounding the walls of the model. This inflation layer allows for more accurate calculations and results near the boundary of a flow field. The initial mesh structure for both the functioning and malfunctioning valve is shown in Figure 2.6 and Figure 2.7 respectively. Additional mesh refinement was done once the mesh was imported into Fluent 18.1, using the region-based adaptation throughout the entire domain. A mesh independence comparison was also done to determine the refinement necessary for accurate results and a lower computation time.

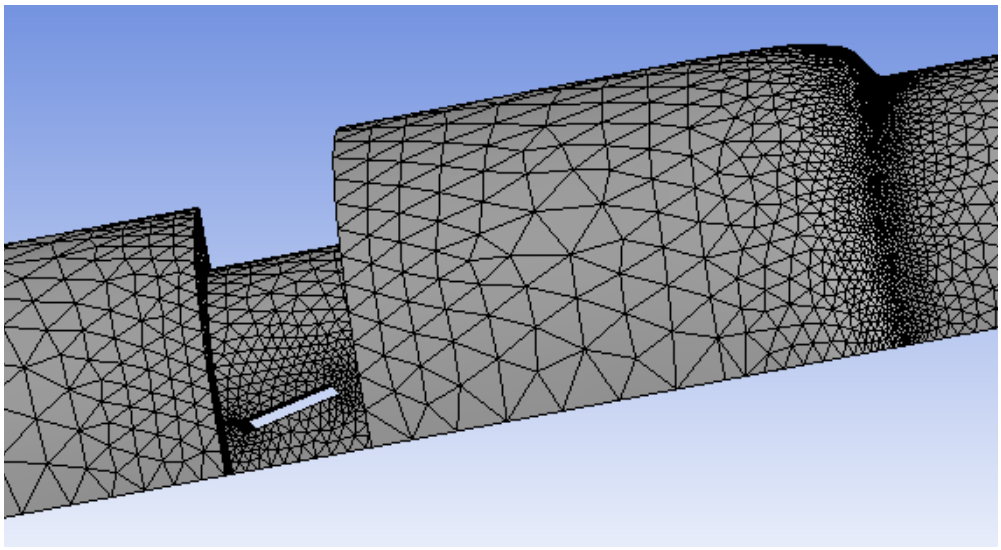

Figure 2.6 Functioning valve system mesh

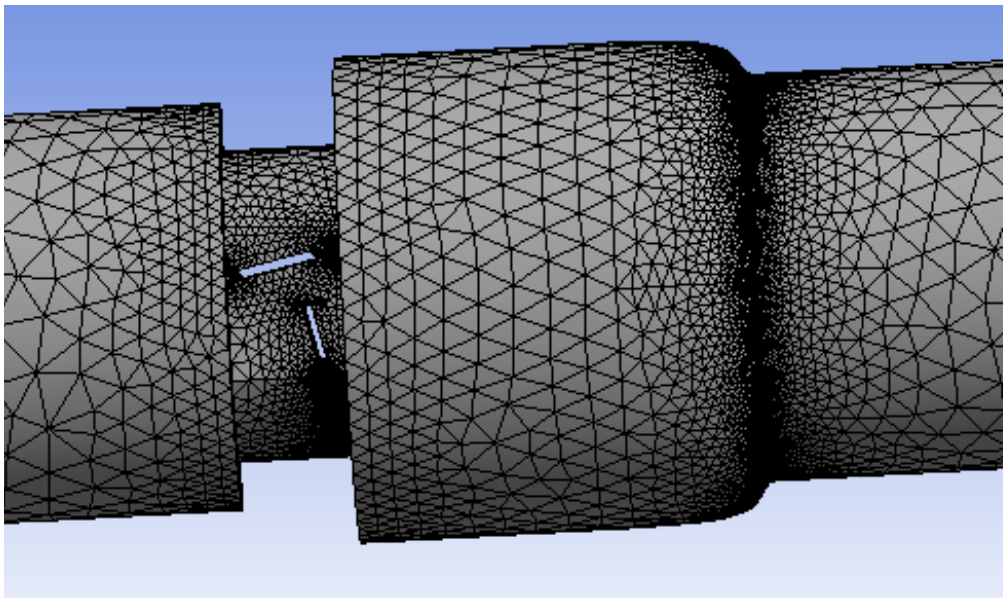

Figure 2.7 Malfunctioning valve system mesh

2.3 Fluent Simulations and Model Validation

The mesh files were imported into ANSYS Fluent and, simulations of different flow conditions conducted. To set up the actual flow simulation, a variety of initial parameters need to be set. These include models, cell zone conditions (solid vs. fluid and material), boundary conditions, and methods. The model selection was done based on a comparison with literature results. The cell zone is the volumetric zone of the model, which was set to "fluid." The boundary conditions are set for all of the surfaces in the model. The inlet was set to mass flow, the outlet to outflow (setting used when the conditions of the outlet are not known), the two planes of symmetry to symmetry, and all other surfaces were set to no-slip walls. For methods, the SIMPLE pressure-velocity coupling scheme, Green-Gauss cell based gradient, and standard pressure were used. The order of the momentum, turbulent kinetic energy, and specific dissipation rate was also determined using the comparison with literature results. In all cases, blood was considered Newtonian and homogenous as has been the standard practice with the majority of previous research studies[58, 70].

In the CFD simulations of fluid flow, a series of equations (Navier-Stokes) are solved for various points throughout the fluid. In this case, these equations include the continuity equation for incompressible flow (Equation 2.1) and mass flow equation (Equation 2.2). U_i and U_j are the instantaneous velocity in the i and j directions, x_i and x_j are coordinate directions, ρ is density, p is pressure, and ν is kinematic viscosity. Using the finite volume a method, each of the equations are integrated over each of the mesh cells to create a system of algebraic equations to solve.

$$\frac{\partial U_i}{\partial x_i} = 0 \qquad \textbf{Equation 2.1}$$

$$\frac{\partial U_i}{\partial t} + U_j \frac{\partial U_i}{\partial x_j} = \frac{1}{\rho}\frac{\partial p}{\partial x_i} + \nu \frac{\partial^2 U_i}{\partial x_j \partial x_j} \qquad \textbf{Equation 2.2}$$

For turbulence modeling, the k-ω SST turbulence model solves transport equations for the turbulent kinetic energy k, and ω, which is ε/k (where ε is the turbulent dissipation rate). In the equations, μ is viscosity, μ_t is turbulent viscosity, σ_k is the turbulent Prandtl number for k, G_k is the generation of k due to the mean velocity gradients, Y_k is the dissipation of k due to turbulence, σ_ω is the turbulent Prandtl number for ω, G_ω is the generation of ω, Y_ω is the dissipation of ω, and D_ω is the cross diffusion term.

$$\frac{\partial}{\partial t}(\rho k) + \frac{\partial}{\partial x_j}(\rho k U_j) = \frac{\partial}{\partial x_j}\left[\left(\mu + \frac{\mu_t}{\sigma_k}\right)\frac{\partial k}{\partial x_j}\right] + G_k - Y_k \qquad \textbf{Equation 2.3}$$

$$\frac{\partial}{\partial t}(\rho \omega) + \frac{\partial}{\partial x_j}(\rho \omega U_j) = \frac{\partial}{\partial x_j}\left[\left(\mu + \frac{\mu_t}{\sigma_\omega}\right)\frac{\partial \omega}{\partial x_j}\right] + G_\omega - Y_\omega + D_\omega \qquad \textbf{Equation 2.4}$$

Steady flow simulations are commonly used for modeling blood flow through heart valves[71-74]. While these simulations are beneficial for simplified and efficient modeling of very complex systems, they do have their limitations. The simulations do not fully account for the in-vivo pulsatile flow that occurs through heart valves, nor does it take into account the changes that occur in turbulent flow over time. However, this research focuses on the highest level of turbulence, or the peak of systolic flow through the heart valve. This rate is used as the steady flow condition for blood damage comparison. The Fluent software also takes the change over time into account by giving time-averaged results of the characteristics of the flow.

For initial literature comparisons and results, fluid properties in the simulation matched values for Hutchinson's experimental system[68], a kinematic viscosity of 1.57 x 10^{-6} m^2/s and a density of 1796 kg/m^3. The purpose of these runs was to develop validated computational methods before carrying out simulations of blood flow through

the valve. Results were actually compared to those of Blackmore et al., who with the same research group, ran large eddy simulations (LES) based on their physical experimentation[75]. They trusted the detailed velocity profile from the LES model over the physical experimentation because of issues with PIV, including the scarcity and settling of the PIV seed particles in the fluid, preventing the detection of flow separation around the leaflets[75].

Because their computation results were presented in a plot, points were digitized from the graph using a free, open source software (WebPlotDigitizer). This software allows one to upload a figure, and based on the scaled axes, pull data points from that figure. The data points taken from the figure were used as experimental points for error analysis of computational results. These points do not directly coincide with the points from the Fluent models, so the points taken from WebPlotDigitizer were used to create equations, which could be used to calculate what the experimental results would have been for the specific data points used in the Fluent models.

For the most accurate results, half of the plot (as the results are symmetric) was split into four different lines, each with its own polynomial fit; the composite provided a representation of the velocity profile in a plane aligned with the centerline and perpendicular to the plane of the valve (Figure 2.8). To determine the degree of each polynomial, lines of best fit from polynomial regression of degrees from n=1 to n=6 were generated. The root mean square errors of the predictions of the polynomial equations compared to the digitized literature data were plotted and compared for each of the four lines (Figure 2.9). The root mean square error data is provided in Table 2.2. The 2^{nd} order polynomials were selected for the first three lines, and a 4^{th} order

polynomial was selected for the fourth line. Table 2.3 provides the selected equations. These were determined to be the polynomials, not necessarily with the absolute lowest error, but where the error begins to plateau, preventing overfitting of the data.

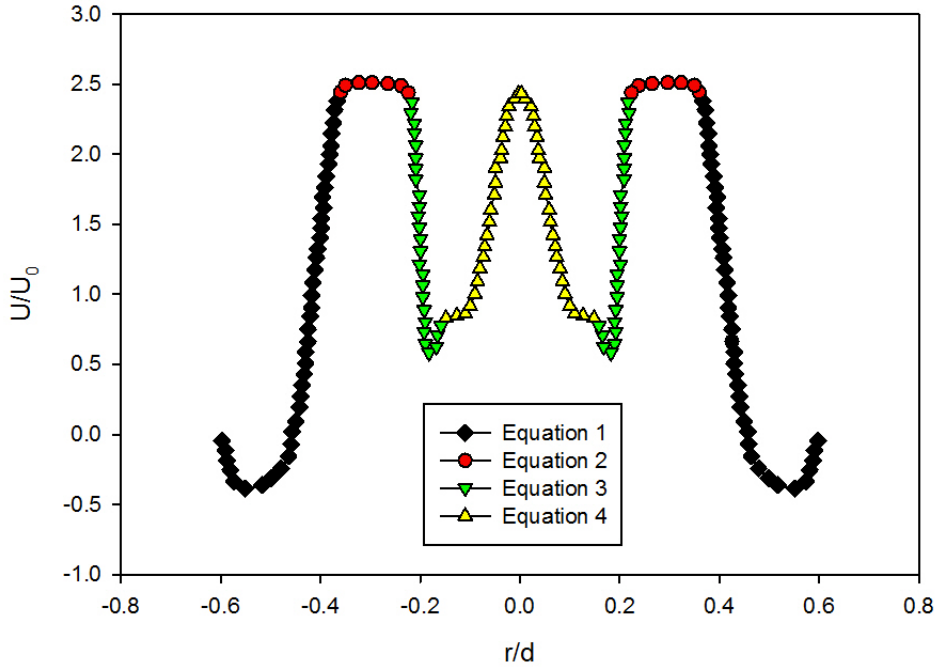

Figure 2.8 Split of literature velocity data[75] into 4 sets that created 4 different equations as seen in Table 2.2 (with one positive and one negative of each)

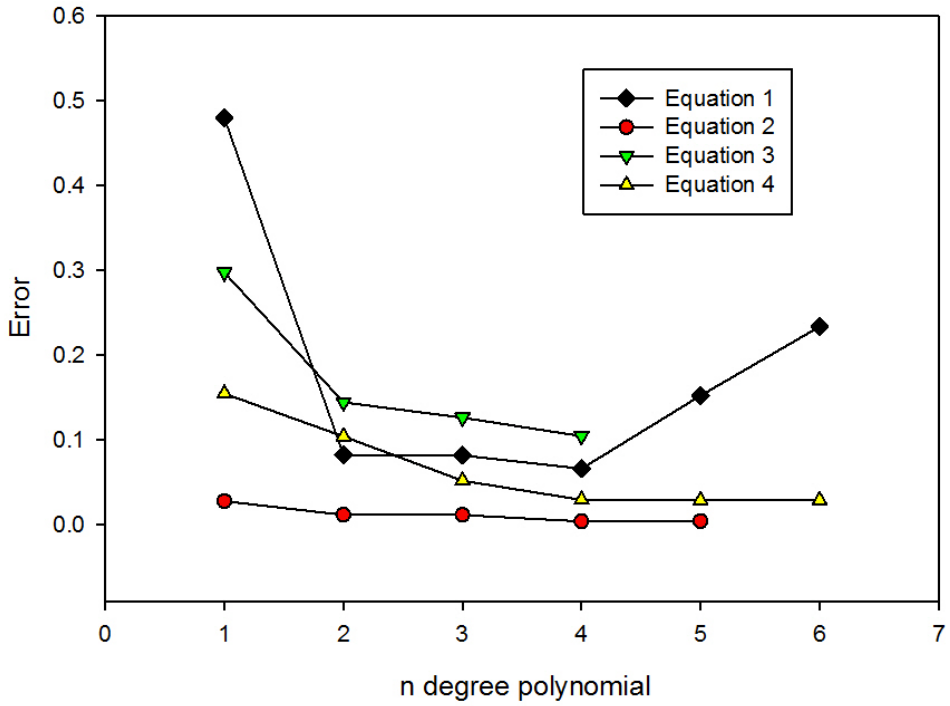

Figure 2.9 Plot of errors of polynomial lines of best fit for each of the four equations in Table 2.2

Table 2.2 Root mean square error data for polynomial lines of best fit

n-polynomial	1st Equation	2nd Equation	3rd Equation	4th Equation
1	0.48	0.028	0.30	0.15
2	0.083	0.012	0.14	0.10
3	0.082	0.012	0.13	0.052
4	0.066	0.0042	0.10	0.030
5	0.15	0.0043		0.029
6	0.23			0.029

Table 2.3 Selected polynomial lines of best fit*

1st Equation	$y = 117.93x^2 + 124.77x + 32.451$ (-0.60 ≤ x ≤ -0.38 and 0.38 ≤ x ≤ 0.60)
2nd Equation	$y = -14.525x^2 - 8.5403x + 1.2643$ (-0.38 < x ≤ -0.23 and 0.23 ≤ x < 0.38)
3rd Equation	$y = 946.17x^2 + 325.65x + 28.598$ (-0.23 < x ≤ -0.15 and 0.15 ≤ x < 0.23)
4th Equation	$y = -18{,}138 * x^4 - 6{,}769.1x^3 - 745.31x^2 - 10.32x + 2.394$ (-0.15 < x ≤ 0.00 and 0.00 ≤ x < 0.15)

*Where y represents the velocity (U/U_0) as a function of radial position (r/d) x.

2.4 Model Selection

2.4.1 Turbulence Model Selection

Turbulence simulations require selection of a mathematical model to represent features of the flow. Fluent simulations were run using both the k-ε turbulence model with enhanced wall function and k-ω SST turbulence model with curvature and low-Re corrections. For both models, a run was done with 1st and 2nd order upwind discretization schemes. The velocity profiles resulting from each of these models were compared with the velocity profile presented by Blackmore et al. (Figure 2.10)[75]. The calculated root mean square and mean absolute errors of each of the models are provided in Table 2.4. As the 1st order k-ω SST model has the lowest error, it was used for all of the subsequent simulations.

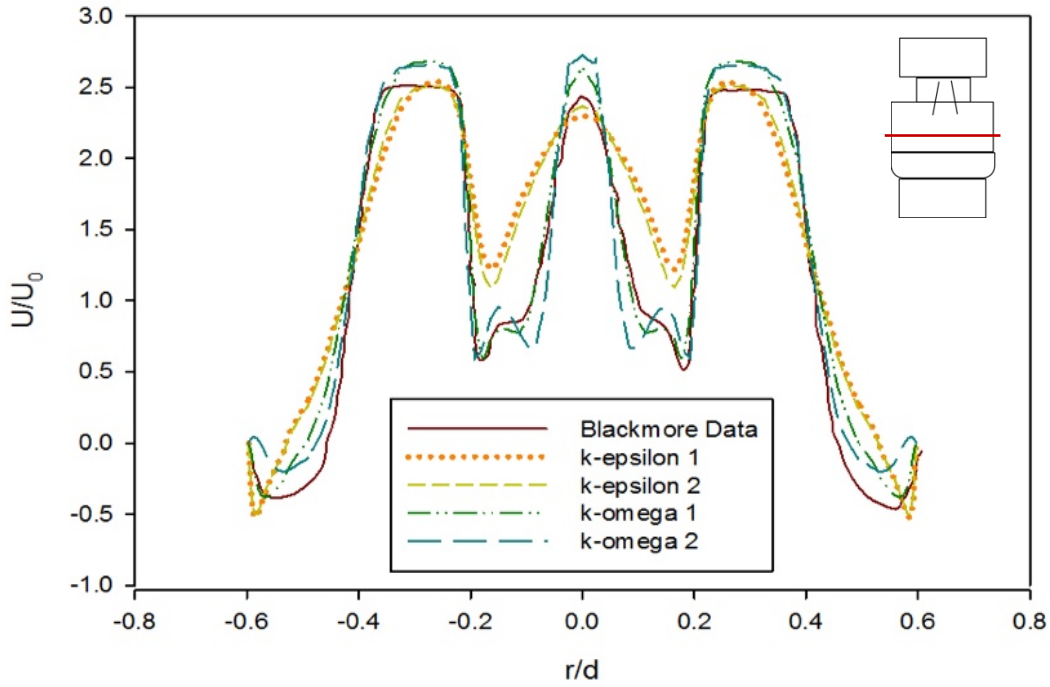

Figure 2.10 Comparison of time-averaged velocity profiles at x = 414 mm (using the Hutchinson run settings[76] with an inlet velocity of 0.445 m/s) from various turbulence model predictions

Table 2.4 Table of root mean square and mean absolute errors for turbulence models

	k-epsilon 1	**k-epsilon 2**	**k-omega 1**	**k-omega 2**
Mean Absolute Error	0.374	0.329	0.208	0.104
Root Mean Square Error	0.109	0.086	0.016	0.028

2.4.2 Mesh Density Selection

Once the model was selected, a mesh independence analysis was done by refining the mesh grid. Refinement was done using the region adaptation function in Fluent until the difference in mesh sizing did not show a significant difference in simulation results. The initial mesh created using the meshing software in ANSYS

Workbench is considered the 'coarse' mesh, the mesh with only an a single round of region-based refinement is the 'medium' mesh, and the mesh with a second round of region-based refinement is the 'fine' mesh. The mesh sizing numbers are summarized in Table 2.5.

Table 2.5 Table of mesh sizes at different densities

Mesh	Cells	Faces	Nodes
Coarse	117,950	263,649	37,829
Medium	943,600	2,080,556	284,342
Fine	7,548,800	16,529,904	2,204,660

To determine the best mesh to use, variables were compared at various cuts along the length of the geometry and axially within the flow field. For example, axial cuts of total pressure (Figure 2.11) and velocity magnitude (Figure 2.12) show a distinct difference in shape between the coarse and medium mesh, but that same distinction is not seen between the medium and fine meshes. This same trend is seen in a comparison of the KLS values on the centerline 405 mm from the inlet of the geometry, which is within the valve and crosses the leaflets (Figure 2.13) as well as the comparisons of velocity magnitude and turbulence dissipation rate on the centerline 395 mm from the inlet, which is 5 mm before the valve starts (Figure 2.14 and Figure 2.15). Error was also compared between the meshes. For example, Table 2.6 shows a comparison of the mean absolute percentage errors for the axial cuts of total pressure. The error between the medium and fine meshes (4.43%) is significantly lower than between the coarse and medium meshes (12.26%) or coarse and fine meshes (13.23%), supporting the fact that there is not a significant difference in simulations results between the medium and fine

meshes. Because the medium mesh had less cells (meaning a decreased calculation time), iteratively converged to lower residual levels, and did not show a high percent difference from the fine mesh, it was selected as the mesh density.

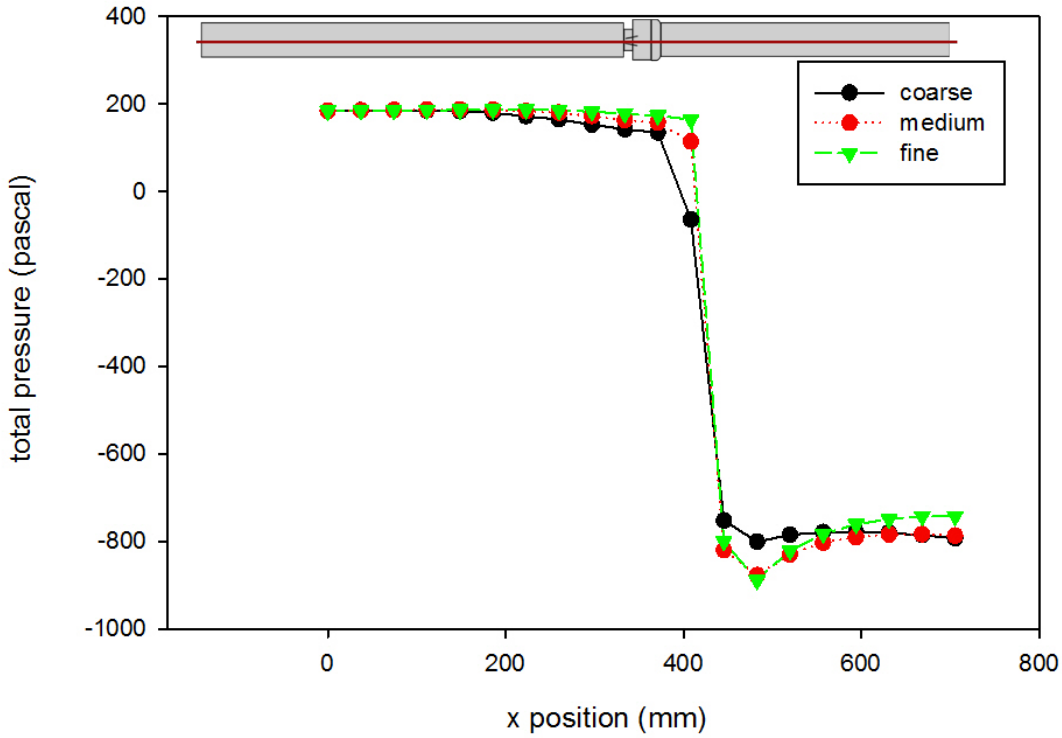

Figure 2.11 Grid independence analysis for total pressure (using the Hutchinson run settings[76] with an inlet velocity of 0.445 m/s)

Table 2.6 Mean absolute percentage error comparison of mesh densities for the axial cut of total pressure

Coarse and Medium	Coarse and Fine	Medium and Fine
12.26%	13.23%	4.43%

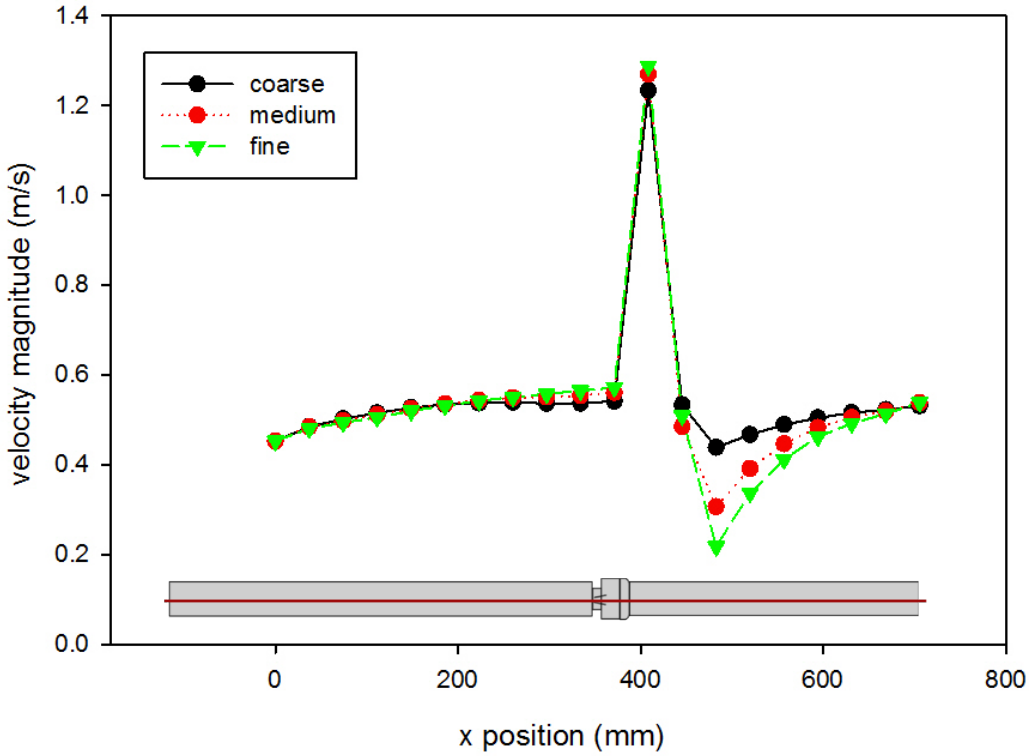

Figure 2.12 Grid independence analysis for velocity magnitude (using the Hutchinson run settings[76] with an inlet velocity of 0.445 m/s)

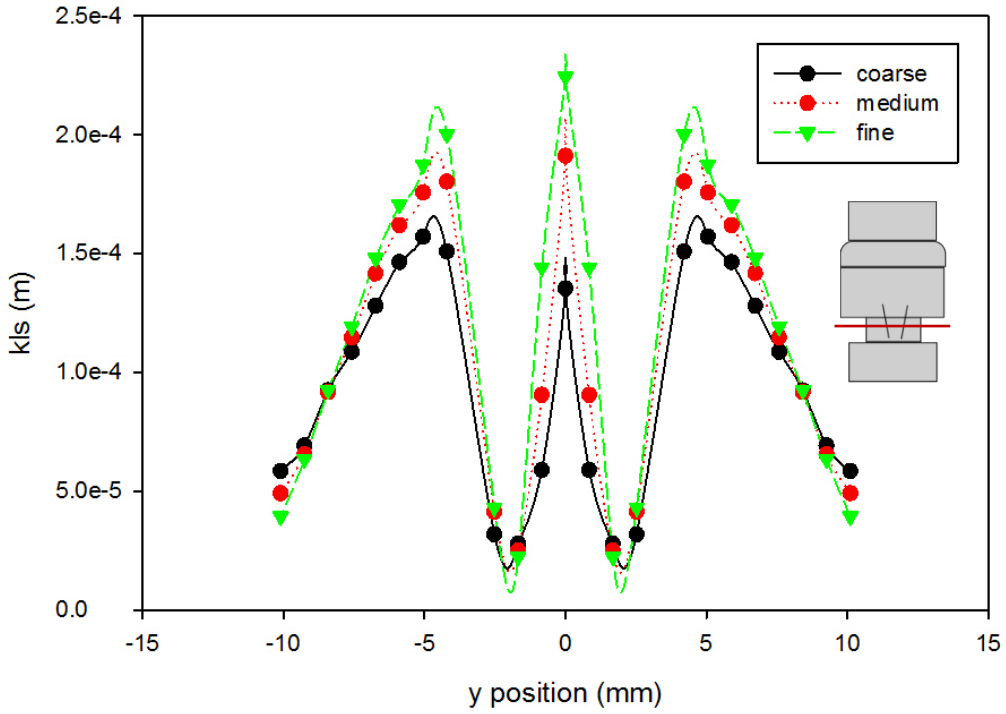

Figure 2.13 Grid independence analysis for KLS at 405 mm downstream of the inlet (using the Hutchinson run settings[76] with an inlet velocity of 0.445 m/s)

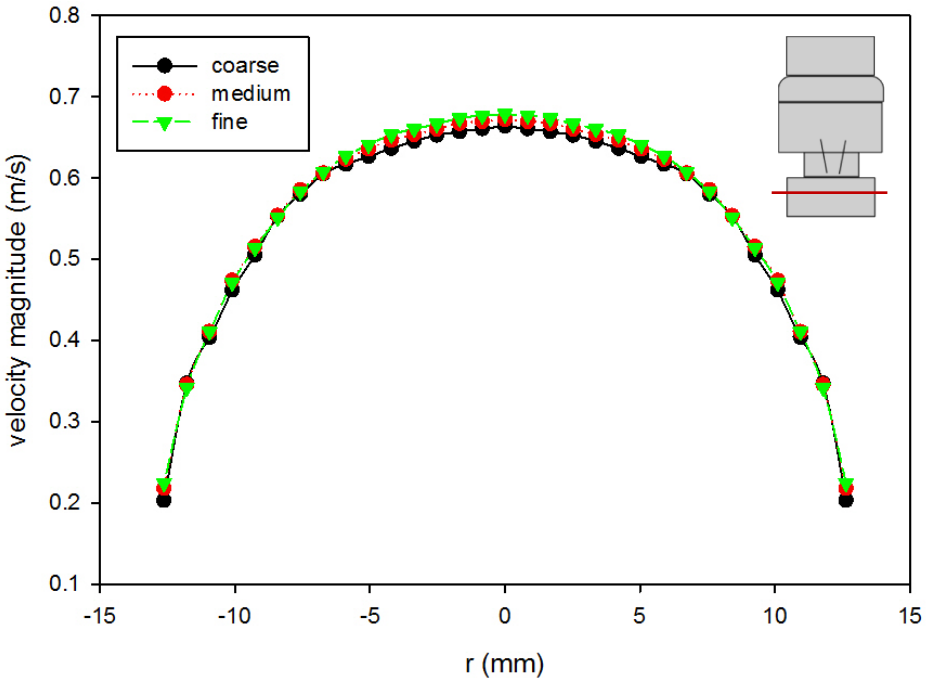

Figure 2.14 Grid independence analysis for velocity magnitude at 395 mm downstream of the inlet (using the Hutchinson run settings[76] with an inlet velocity of 0.445 m/s)

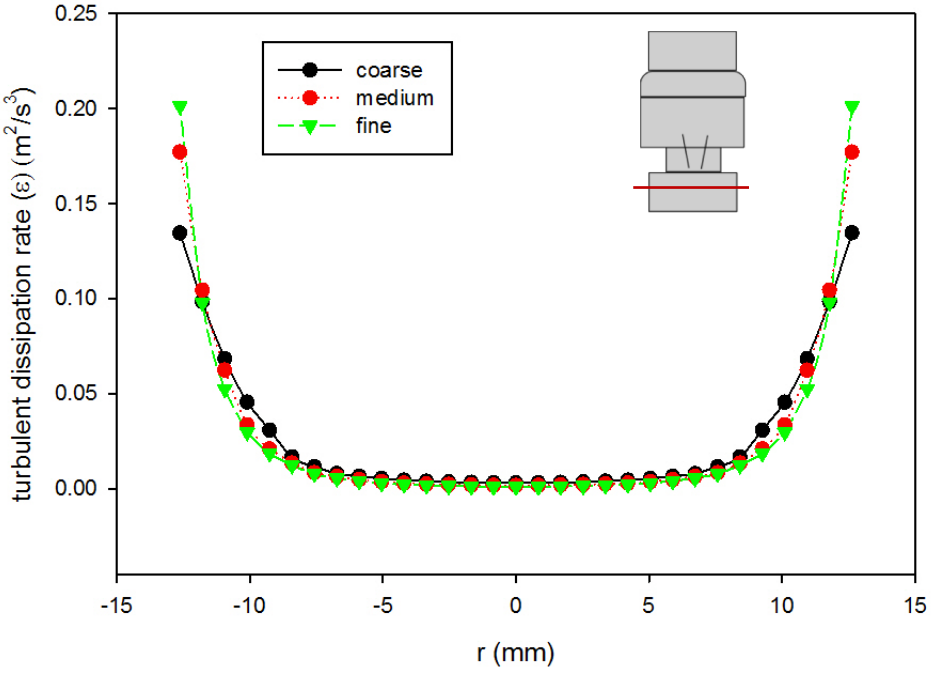

Figure 2.15 Grid independence analysis for turbulent dissipation rate at 395 mm downstream of the inlet (using the Hutchinson run settings[76] with an inlet velocity of 0.445 m/s)

The literature comparisons were done at a Reynolds number of 7600, which based on the given viscosity, density, and diameter, gave an inlet velocity of 0.445 m/s[76]. This translates into a mass flowrate of 0.451 kg/s, or 0.113 kg/s for the abridged representation of the symmetric functioning valve and 0.226 kg/s for the abridged malfunctioning valve because each only models a quarter and half of the overall flow field. Based on agreement with Hutchinson and Blackmore's work, the medium grid refinement (943,600 cells) and the k-ω SST turbulence model with curvature and low-Re corrections were selected for the simulations of blood flow through the valve.

2.5 KLS Calculations and Eddy Analysis

After results were compared with the literature data using settings from Hutchinson's experiment[68], new runs were done using a fluid physiologically similar to blood with a viscosity of 0.002 Pa-s and a density of 1050 kg/m^3, as was used by Ozturk et al. in the CFD simulations used to create the new hemolysis equation[62]. These simulations with blood were used to obtain KLS distributions in the flow through the valve for eddy analysis and hemolysis predictions. The flowrates in this case were set to peak systolic flow, when turbulence is at its highest and blood is most likely to be damaged. Peak velocity of blood through heart valves in systolic flow has been used or cited as anywhere from 1.0-1.8 m/s, and in cases is found to be higher through artificial valves[38, 64, 66, 77]. General values of 1.25 m/s and 1.5 m/s were selected for these simulations.

Cross-sectional surfaces were created axially through the heart valve, each .5 mm apart. The surfaces were created along the length of the flow field that contained eddies of 10 μm or smaller. For each surface, the KLS values were calculated by Fluent using a user-defined equation (Equation 1.2). The total surface areas of spheres of diameters equal to the KLS values were calculated in 1 unit intervals (a unit being 1 μm) up to a diameter of 10 μm. The region of a particular KLS size range can be determined between two consecutive surfaces, which when multiplied by the distance between the two surfaces, will determine the volume of the KLS.

The number of eddies (N_{eddy}) of each size can be found by dividing the total volume of the region made up by eddies of that specific size by the volume of one eddy (V_{eddy}), when the assumption that the eddies are spherical is made (Equation 2.1). Finally, the total surface area of eddies for each KLS value (A_{eddy}) was calculated (Equation 2.2). The total surface areas are then normalized by dividing by the total volume of the region where hemolysis is a concern (the total volume of eddies with a KLS of either 9 or 10 μm or less, depending on the equation). This normalization process allows for the calculations of hemolysis values that are device-independent, to compare across different types of devices, in this case extending to heart valves. This allows for the calculation of hemolysis expected per volumetric unit for the region where hemolysis occurs. Additional information about KLS and eddy calculations are included in the Appendix.

$$V_{eddy} = \frac{4}{3}\pi\left(\frac{KLS}{2}\right)^3 \qquad \textbf{Equation 2.5}$$

$$A_{eddy} = N_{eddy} * 4\pi\left(\frac{KLS}{2}\right)^2 \qquad \textbf{Equation 2.6}$$

It is worth mentioning that a cell-free layer may exist near a wall where RBCs are excluded and would not encounter eddies present in that region. While there are some regions of hemolysis that occur within the length of one or two blood cells from the wall, much of the hemolysis occurs in regions within the length of ten or more blood cells from the wall or off the wall entirely. Also, these cell-free layers are generally only observed for laminar flow and only significant in microvessles, becoming negligible with respect to diameter in larger vessels like the one used in this research (which also allows for the assumption of constant viscosity, Newtonian fluid)[78, 79].

3 Results and Discussion

3.1 Velocity Comparison

Velocity characteristics of the functioning and malfunctioning valves were compared using two different fluids. Initially, a test fluid matching the one used by Hutchison[68] was used to develop the comparative system. In subsection 3.1.1, the velocity comparisons for the test fluid were obtained. After computational model validation and initial comparisons, blood was used as the fluid. The velocity results for blood were obtained in subsection 3.1.2. The two fluids are shown in Table 3.1.

Table 3.1 Comparison of two fluids used for CFD modeling

Fluid	**Density (kg/m^3)**	**Kinematic viscosity (m^2/s)**	**Dynamic viscosity (Pa-s)**
Test fluid	1796	1.57 x 10^{-6}	—
Blood	1050	—	0.002

3.1.1 Test Fluid

The inlet velocity profile progression for planes defined by the tube centerline and the midline of the valve leaflet at various axial positions (x = 0, 100, 200, 300, 350, 375 mm from the inlet) are plotted for both the functioning and malfunctioning valves using the Hutchinson run settings and fluid[76] in Figure 3.1 and Figure 3.2. Both profiles show the time-averaged plug flow shape indicative of turbulent flow. Beyond 200 mm, the shape of the profile does not continue to change as drastically, indicating the inlet turbulent flow is fully developed before reaching the heart valve inlet. It also shows that the leaflets do not have an effect on the velocity profile too far upstream of the beginning of the valve.

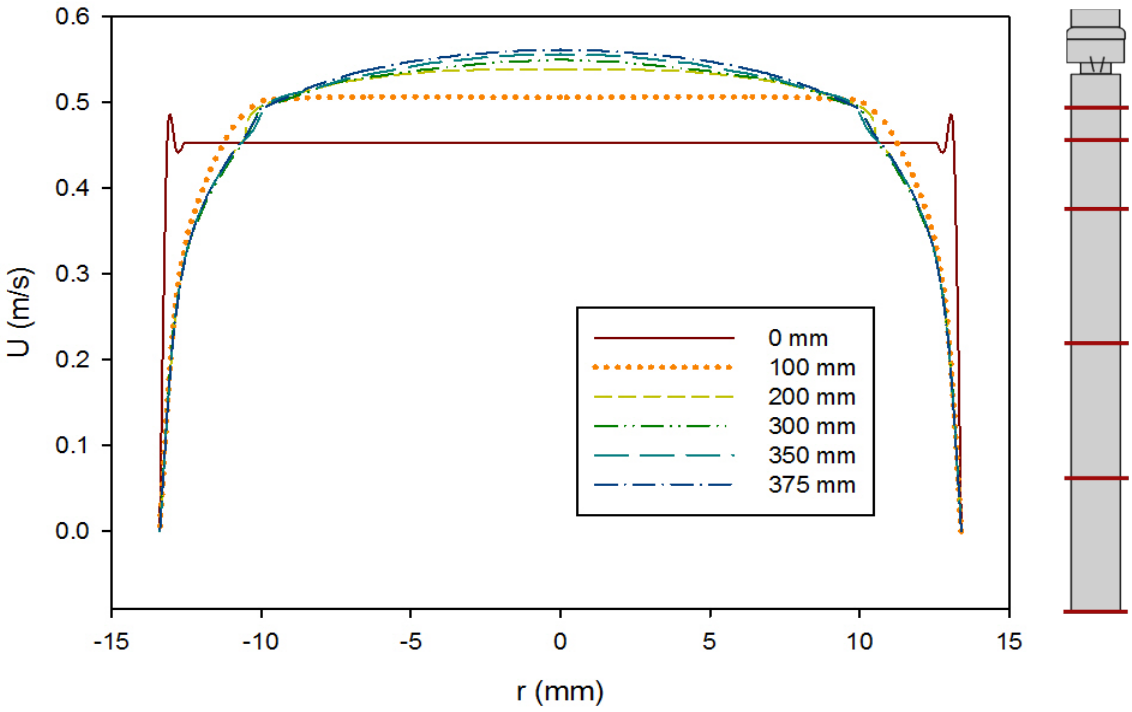

Figure 3.1 Velocity profiles at various axial inlet positions upstream of the valve and leaflets of the functioning valve (using the Hutchinson run settings[76] with an inlet velocity of 0.445 m/s)

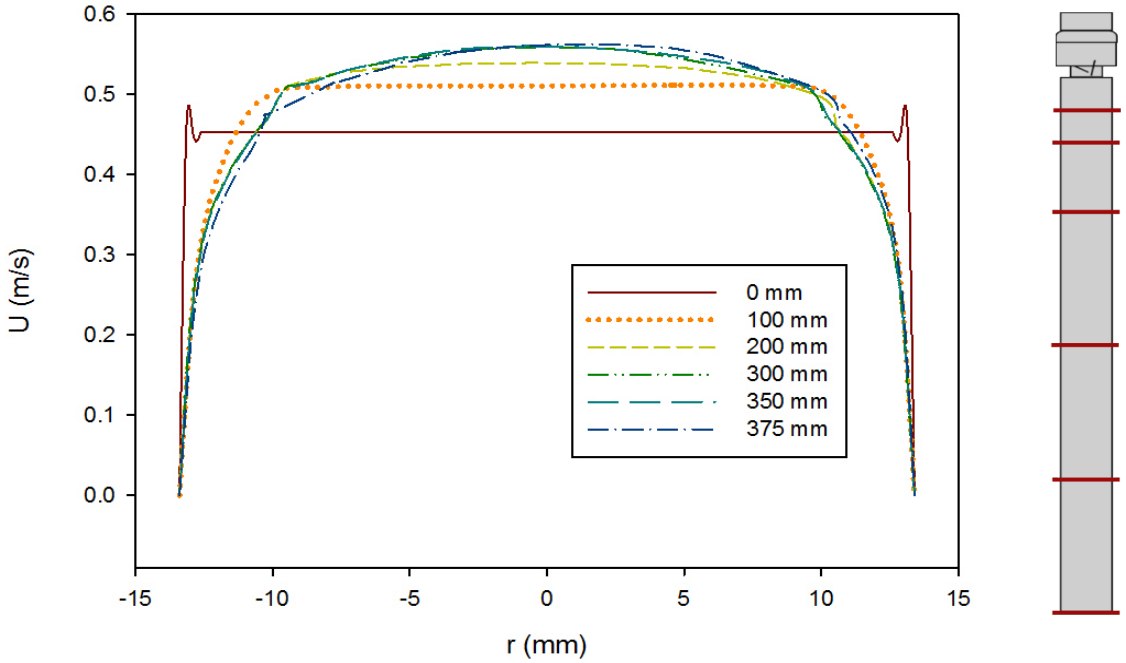

Figure 3.2 Velocity profiles at various axial inlet positions upstream of the valve and leaflets of the malfunctioning valve (using the Hutchinson run settings[76] with an inlet velocity of 0.445 m/s)

A comparison of the velocity profiles for the functioning and malfunctioning valves 375 mm downstream from the inlet (25 mm before the start of the valve) is shown in Figure 3.3. The shape of the profiles match for the functioning and malfunctioning valve, which confirms that both models reached a comparable fully developed turbulent flow. It also means the same velocity profile approached the valve inlet, so the downstream variance in velocity profiles are only caused by the difference between the leaflets and no variance in flow prior to that.

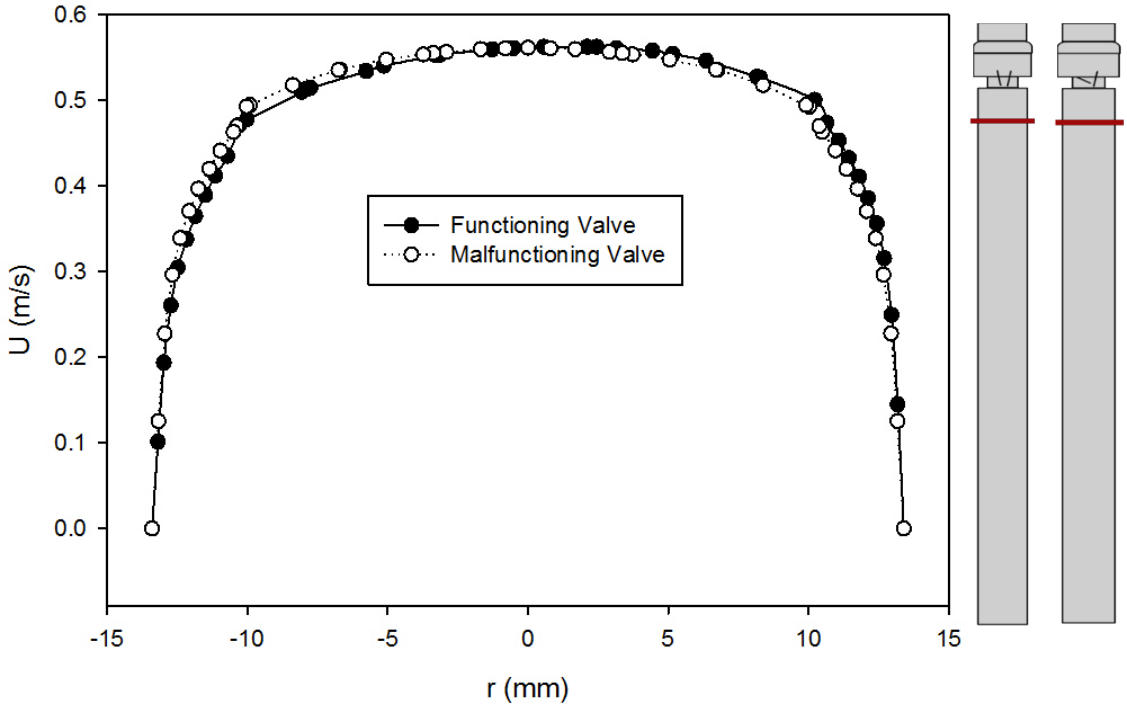

Figure 3.3 Comparison of velocity profiles at x = 375 for the functioning and malfunctioning valves (using the Hutchinson run settings[76] with an inlet velocity of 0.445 m/s)

The velocity profiles within the valve and sinus (x = 400, 410, 420, 430, 440 mm from the inlet) are plotted for the functioning and malfunctioning valves in Figure 3.4 and Figure 3.5. In both cases, the maximums and minimums of the profiles become more extreme before gradually lessening. This is more so true for the functioning valve, as the malfunctioning valve still shows extreme peaks on the side with the functioning leaflet at the last point 440 mm from the inlet. The change in flow shape is more drastic for the malfunctioning leaflet.

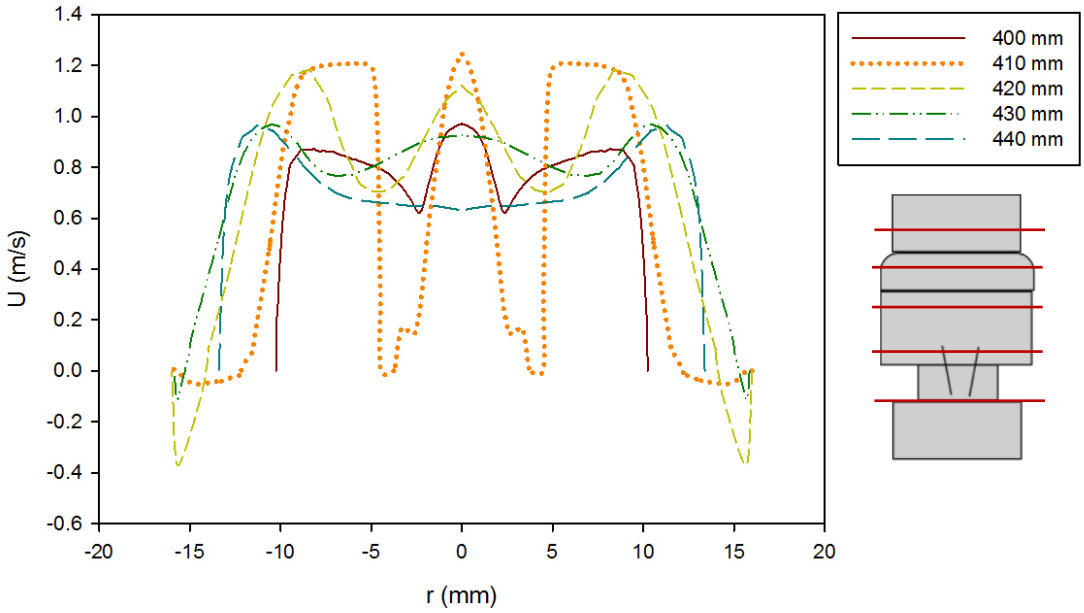

Figure 3.4 Centerline, time-averaged velocity profiles at various axial positions within the valve and sinus regions of the functioning valve (using the Hutchinson run settings[65] with an inlet velocity of 0.445 m/s)

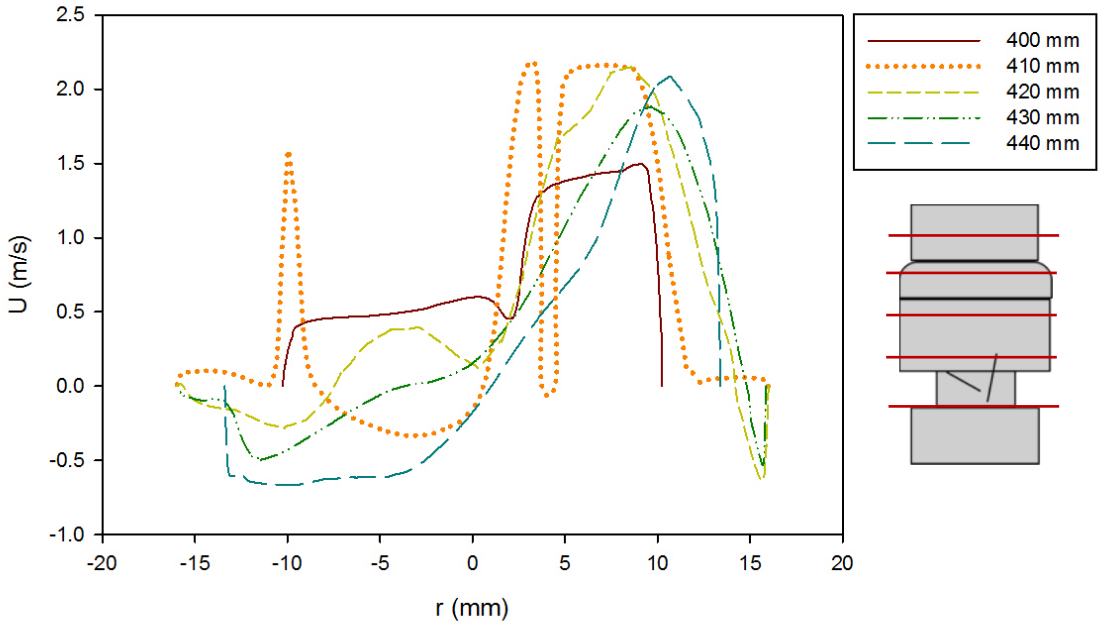

Figure 3.5 Centerline, time-averaged velocity profiles at various axial positions within the valve and sinus regions of the malfunctioning valve (using the Hutchinson run settings[65] with an inlet velocity of 0.445 m/s)

The velocity profiles just past the leaflet tips (at 414 mm downstream of the inlet) are compared for the two valves in Figure 3.6. This point was chosen as it was the location of data from Blackmore et. al.[75] used to select the mathematical model for calculations. The plot shows that the peak velocity just past the leaflets increased from around 1.2 m/s for the functioning valve to 2.1 m/s for the malfunctioning valve. This is expected because when one of the leaflets (the leaflet in the negative y-axis) is closed more of the fluid is forced through the space around a single leaflet, which increases the volumetric flow in that area, increasing the velocity. The dented shape of the profile corresponds with the slanted tip of the leaflet.

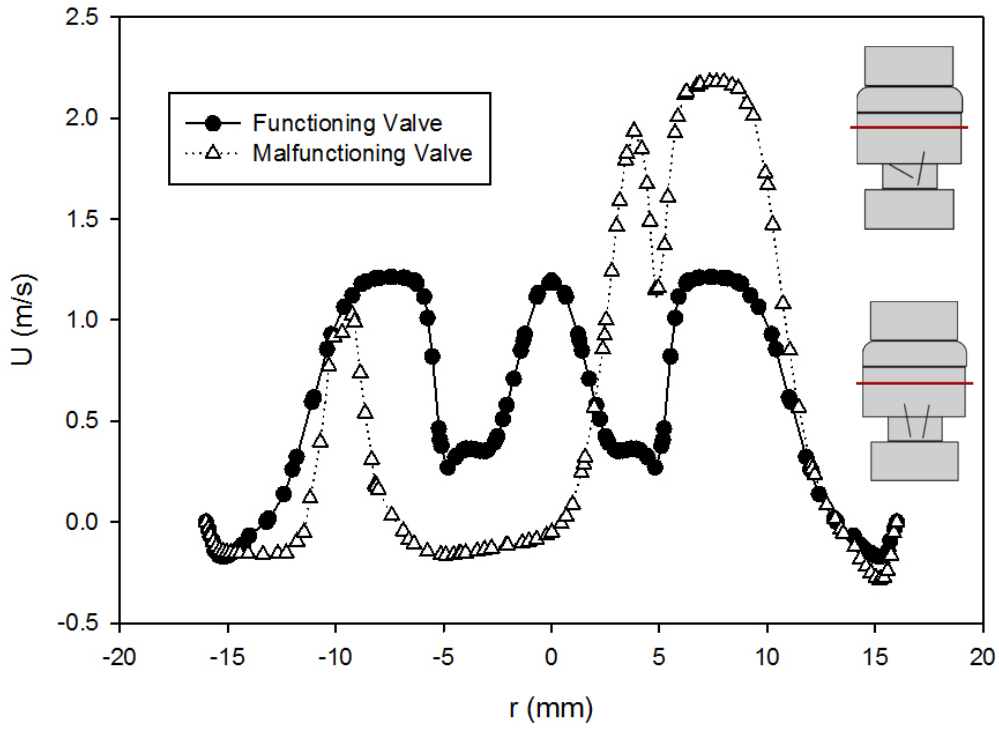

Figure 3.6 Comparison of velocity profiles at x = 414 for the functioning and malfunctioning valves (using the Hutchinson run settings[76] with an inlet velocity of 0.445 m/s)

In Figure 3.7 and Figure 3.8 a comparison of varying radial velocity profiles at x = 414 mm from the inlet (r = 0, 2, 4, 6, 8, 9.075 mm from the centerline) for the functioning and malfunctioning valves is displayed. The farther the profiles move from the centerline, the smaller the peaks get. The middle maximum also eventually levels out in both cases, leaving two outer maximums with a minimum in between. This gradual leveling of the profile makes sense because the leaflets are curved at the end, so the longest length of the leaflet in the axial direction is at the centerline and the shortest length is at the valve's edge (z = 9.075 mm). As one moves from the centerline, the length of the leaflet in the axial direction decreases with less impact on the flow.

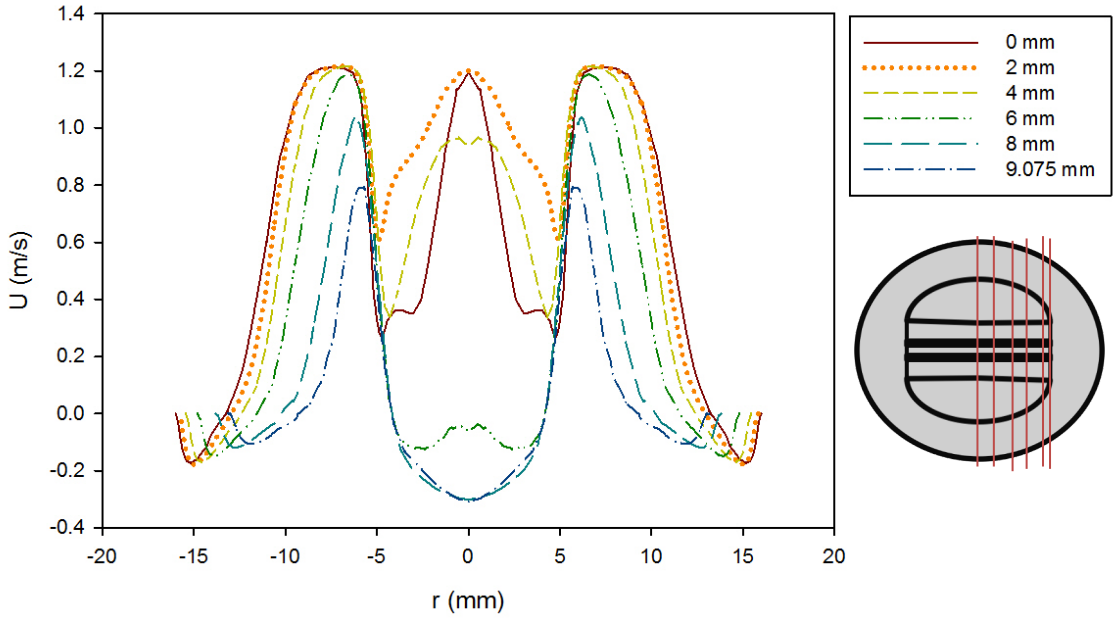

Figure 3.7 Velocity profiles at various radial positions in the sinus at x = 414, for the functioning valve (using the Hutchinson run settings[65] with an inlet velocity of 0.445 m/s)

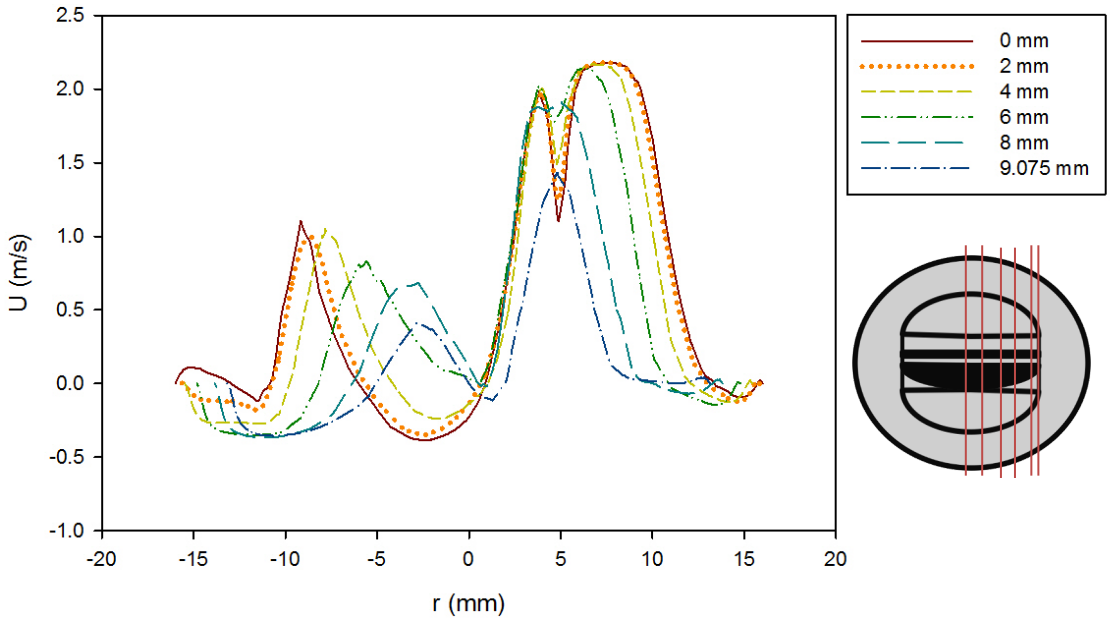

Figure 3.8 Velocity profiles at various radial positions in the sinus at x = 414, for the malfunctioning valve (using the Hutchinson run settings[65] with an inlet velocity of 0.445 m/s)

The velocity profiles downstream of the valve and sinus (x = 450, 500, 550, 600, 650, 700, 705.5 mm from the inlet) are plotted for the functioning and malfunctioning valves in Figure 3.9 and Figure 3.10. As the profiles progress, the shape of the profiles begin to return to plug flow. The velocity profile of the functioning valve regains the fully developed turbulent flow shape beyond 600 mm downstream of the inlet. However, the velocity profile of the malfunctioning valve does not fully regain the fully developed turbulent flow shape by the outlet. Clearly having one mostly closed leaflet in the malfunctioning valve affects the fluid flow much further downstream than the two fully open leaflets of the functioning valve.

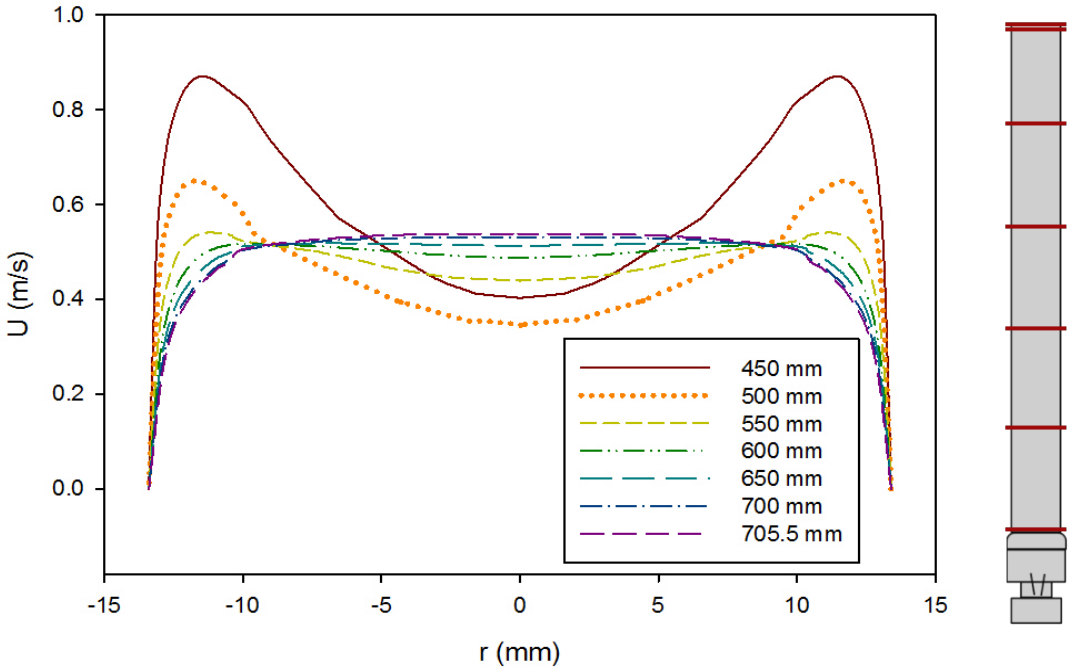

Figure 3.9 Centerline velocity profiles at various axial positions downstream from the valve and sinus of the functioning valve (using the Hutchinson run settings[76] with an inlet velocity of 0.445 m/s)

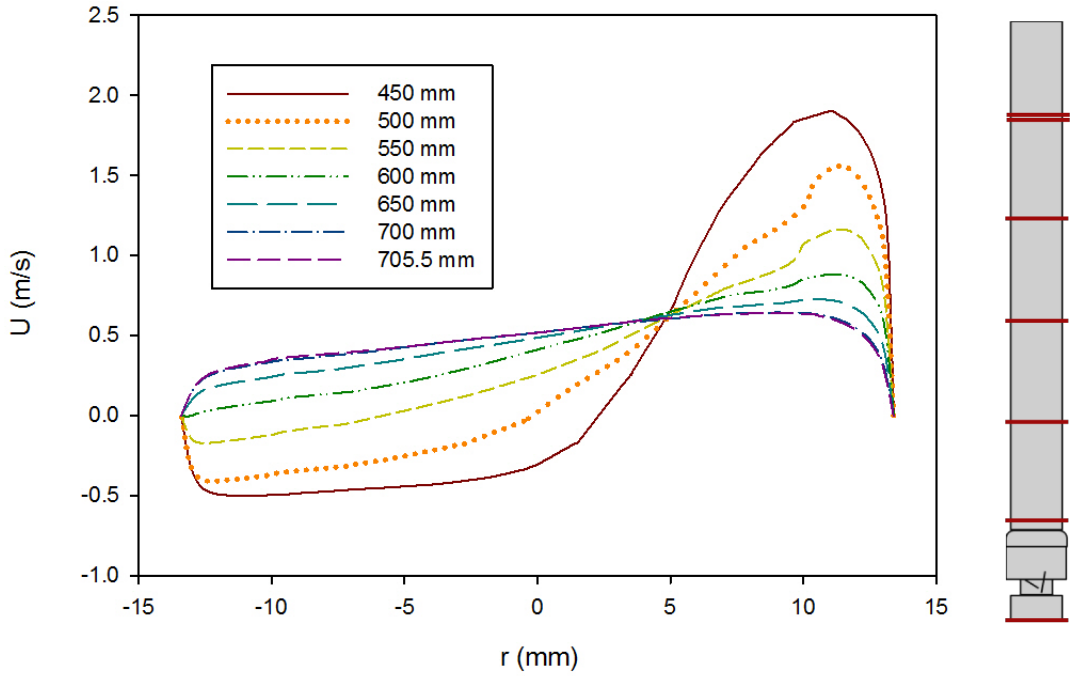

Figure 3.10 Centerline velocity profiles at various axial positions downstream from the valve and sinus of the malfunctioning valve(using the Hutchinson run settings[76] with an inlet velocity of 0.445 m/s)

3.1.2 Blood

After the initial runs using the Hutchinson settings were examined, the runs with blood at 1.25 and 1.5 m/s were analyzed. The contours of x-velocity for the functioning valve with a flowrate of 1.25 and 1.5 m/s are shown in Figure 3.11 and Figure 3.12 respectively. Though the scale of the velocity is higher for the higher flowrate, the contours for both simulations have the same trends. Peak velocity flow is seen in between and just outside of the leaflets. Both contour plots also show backflow and circulation along the inner edge of the leaflets and near the wall after the diameter of the flow field expands from the heart valve channel to the sinus.

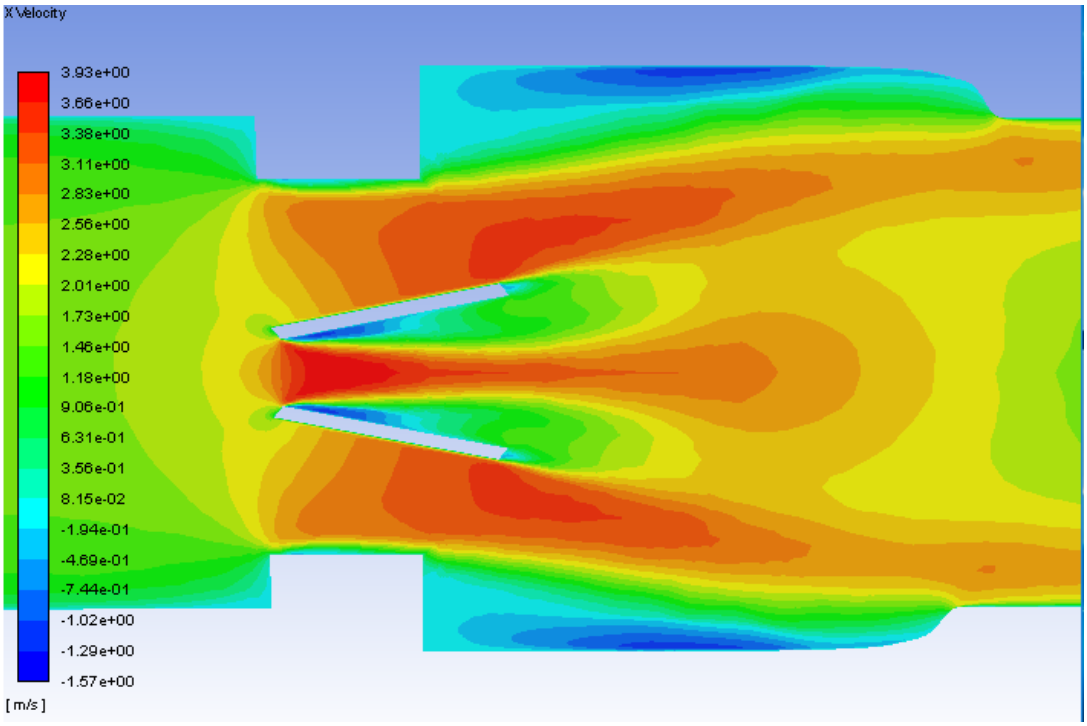

Figure 3.11 Centerline velocity contours on the plane of symmetry for the functioning valve with blood and an inlet velocity of 1.25 m/s

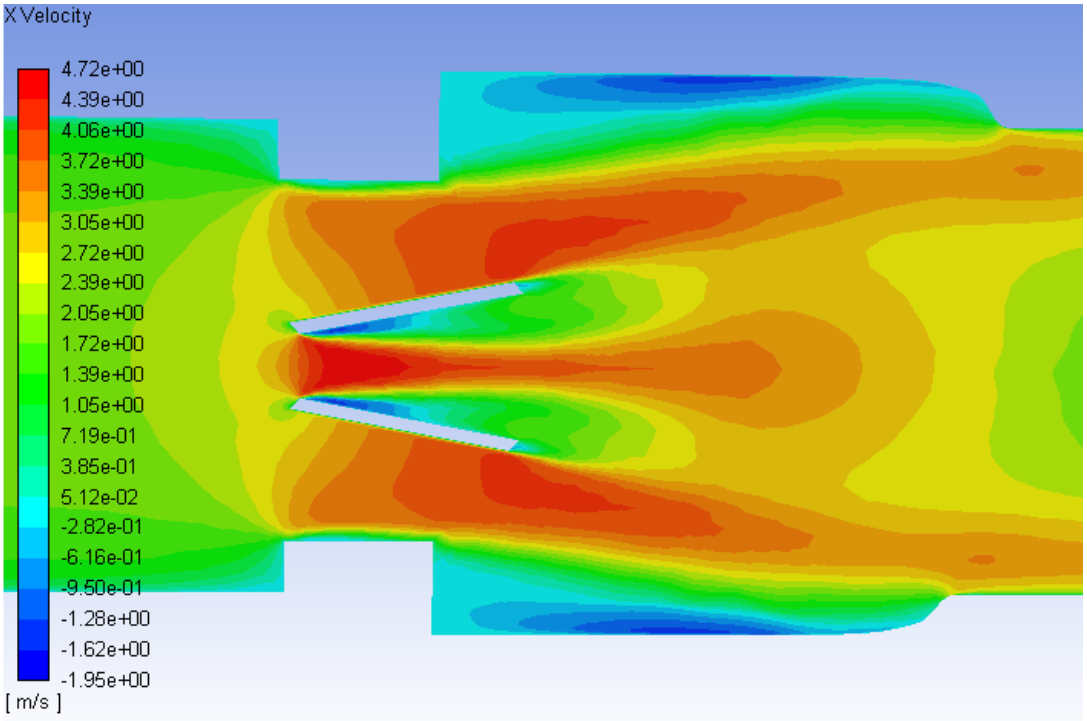

Figure 3.12 Velocity contours on the plane of symmetry for the functioning valve with blood and an inlet velocity of 1.5 m/s

The x-velocity contours for the malfunctioning valve with a flowrate of 1.25 and 1.5 m/s are shown in Figure 3.13 and Figure 3.14. As with the functioning valve, though the scale is higher for the higher flowrate, the trends in the contours are very similar. Unlike the functioning valve, the contours are not symmetric about the centerline. There is a much larger area of high velocity flow around the fully open leaflet, and there is a much larger area of backflow and circulations beyond the mostly closed leaflet. There is still a very small region of high velocity in the small gap between the malfunctioning leaflet and the wall but it does not extend near as far as the high velocity region around the functioning leaflet.

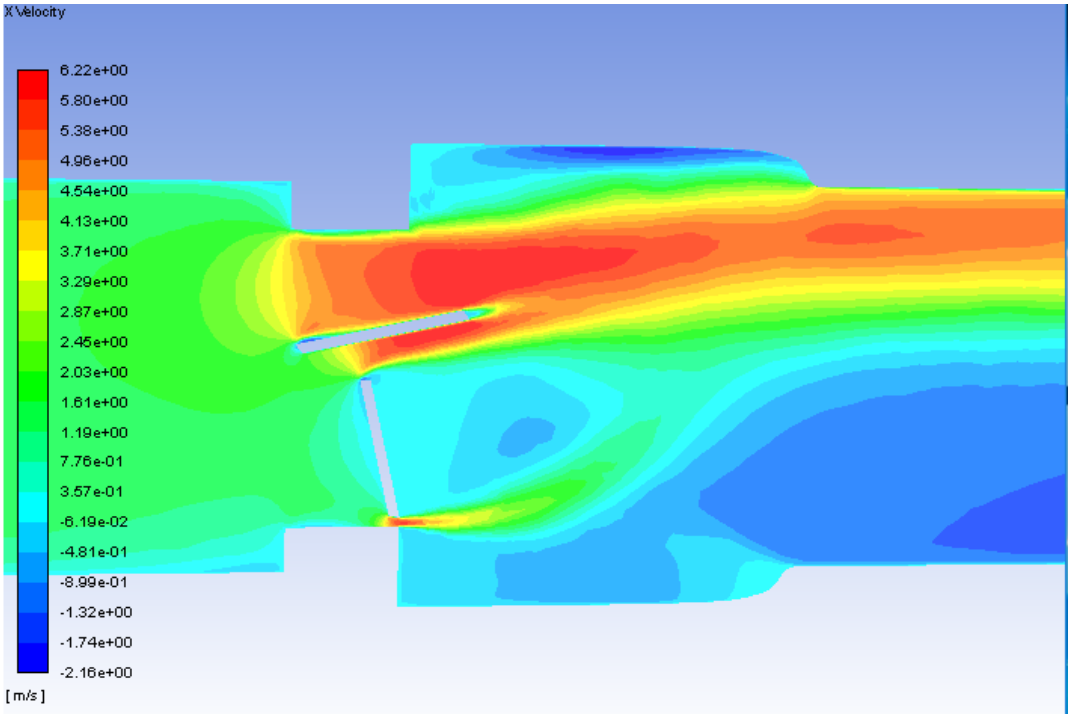

Figure 3.13 Velocity contours on the plane of symmetry for the malfunctioning valve with blood and an inlet velocity of 1.25 m/s

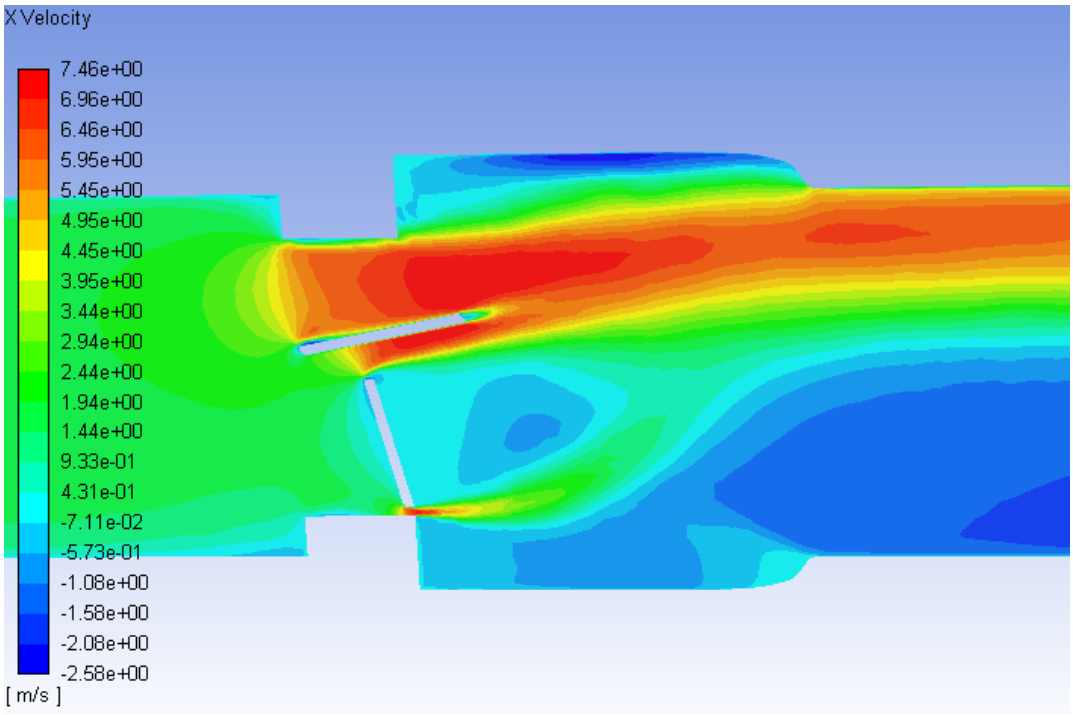

Figure 3.14 Velocity contours on the plane of symmetry for the malfunctioning valve with blood and an inlet velocity of 1.5 m/s

3.2 KLS Calculations and Eddy Analysis

3.2.1 KLS Contours

The eddies of 10 μm diameter or less are of interest in this research, so the contours of eddies of this size were found for the various runs with blood. The volumetric contours of these eddies are shown in Figure 3.15 and Figure 3.17 for the functioning heart valve with a 1.25 and 1.5 m/s inlet velocity respectively. The areas with low KLS values are concentrated near the leading edge of the leaflets or near the wall when the model decreases in diameter (where the inlet meets the valve and where the aortic sinus meets the outlet). A close-up is given of the KLS contours near the valve channel and leaflet for both cases (Figure 3.16 and Figure 3.18). The amount of space taken up by these small eddies clearly increases when the velocity is increased.

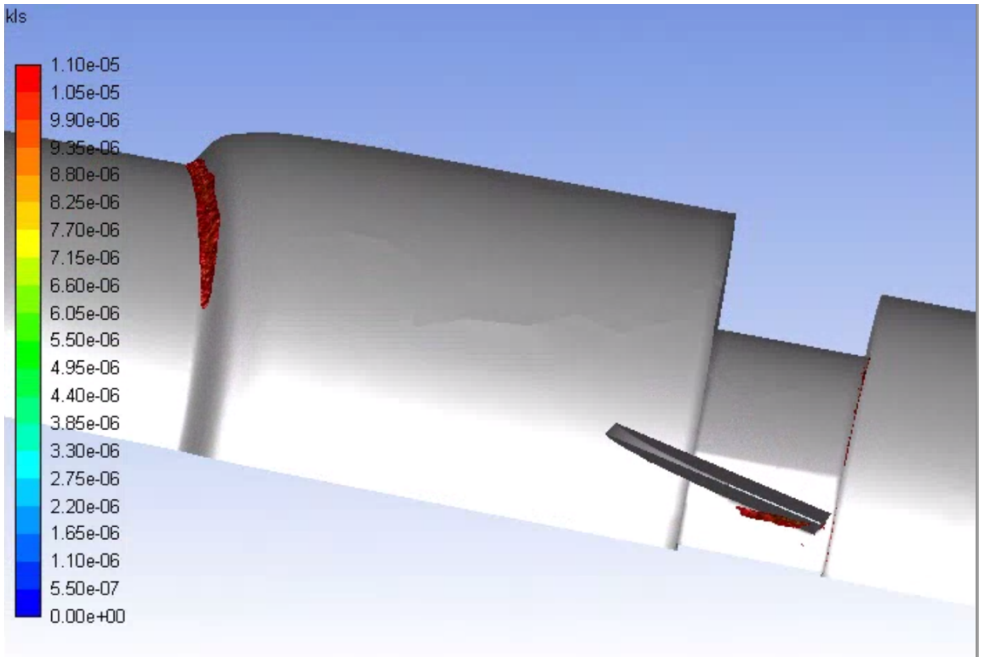

Figure 3.15 Volumetric contours of eddies with low KLS values (KLS ≤ 10 μm) for the functioning valve with blood and an inlet velocity of 1.25 m/s (Note: The view is the inner portion of the valve, so the direction of the model appears reversed.)

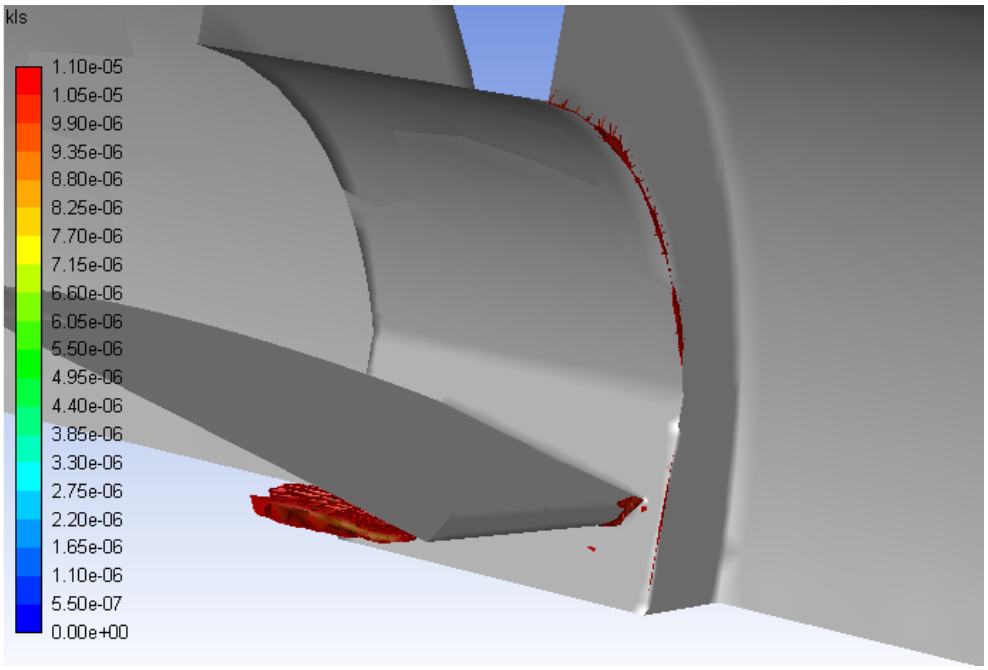

Figure 3.16 A close-up view of the volumetric contours of KLS values near the valve and leaflet in the functioning valve (with blood and an inlet velocity = 1.25 m/s)

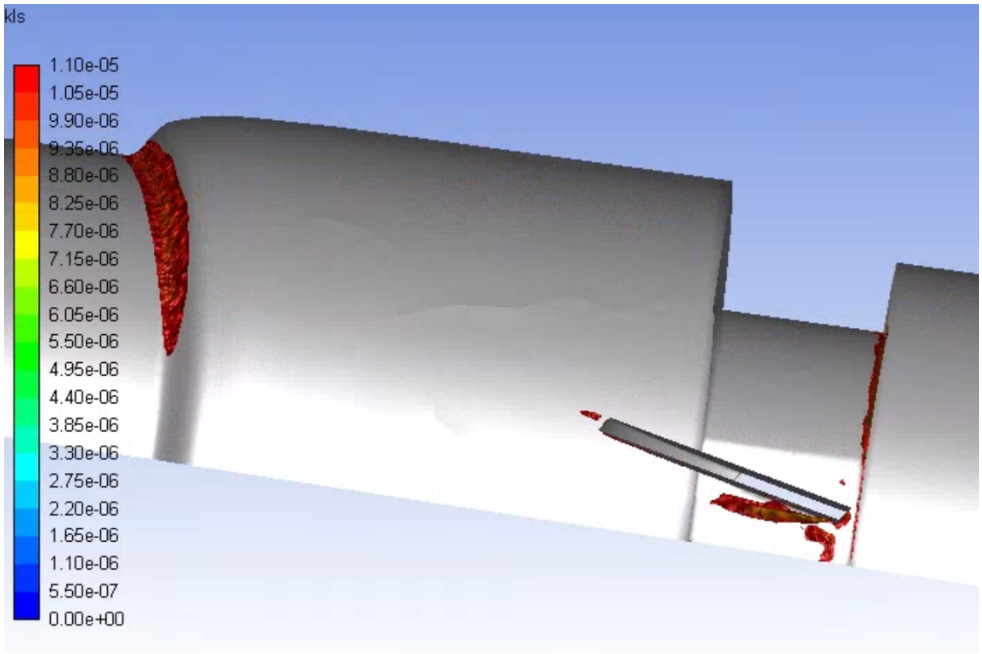

Figure 3.17 Volumetric contours of eddies with low KLS values (KLS ≤ 10 μm) for the functioning valve with blood and an inlet velocity of 1.5 m/s (Note: The view is the inner portion of the valve, so the direction of the model appears reversed.)

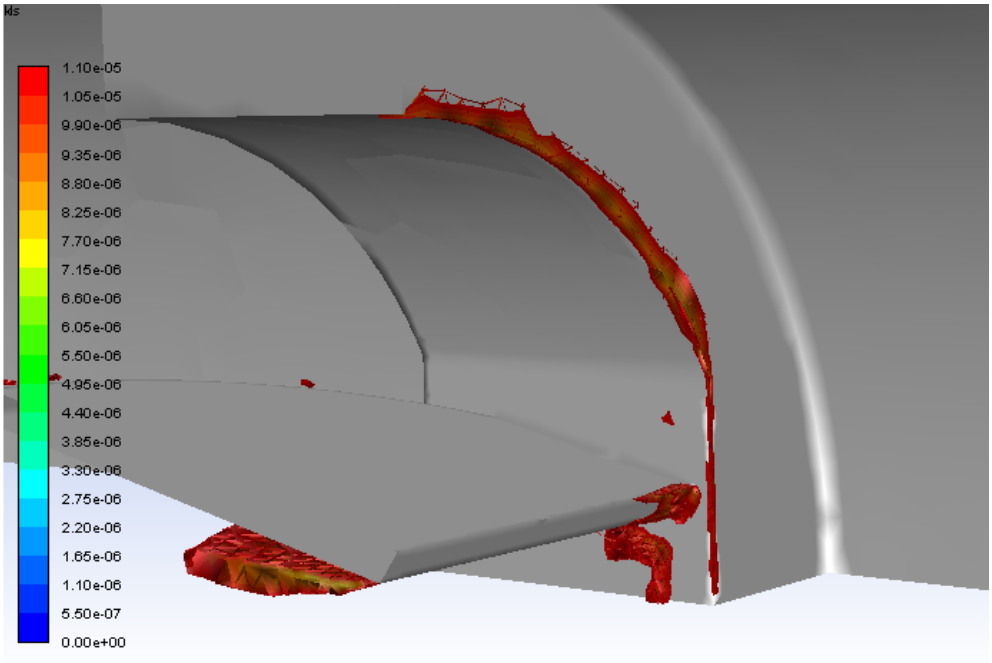

Figure 3.18 A close-up view of the volumetric contours of KLS values near the valve and leaflet in the functioning valve (with blood and an inlet velocity = 1.5 m/s)

Two different angles of the volumetric contours of eddies can be seen in Figure 3.19 and Figure 3.21 for the malfunctioning valve with an inlet flowrate of 1.25 m/s. Similarly, two different angles of the contours for the malfunctioning valve with an inlet flow of 1.5 m/s are presented in Figure 3.23 and Figure 3.25. Eddies are concentrated around the leaflets, around the wall when there is a decrease in the model diameter, and in the spaces between the leaflets and the walls where fluid velocity sharply increases. The eddies concentrated around the wall are on the side of the valve and sinus closer to the functioning leaflet, where the large region of high velocities was seen in the velocity contours. The eddies with the highest intensity (the smallest eddies) are located between the leaflets, just along the surface of the functioning leaflet. Close-ups of the KLS contours near the valve channel and leaflet are shown for both views of the malfunctioning valve with an inlet flowrate of 1.25 m/s (Figure 3.20 and Figure 3.22). The same close-ups of the KLS contours are also shown for the inlet flowrate of 1.5 m/s (Figure 3.24 and Figure 3.26).

As with the functioning valve, when the inlet velocity increased the volume taken up by these small eddies increased in the malfunctioning valve model. At a higher velocity the eddies also continue further along the length of the flow field—from 50 mm downstream of the valve inlet with the 1.25 m/s inlet velocity to and 75 mm downstream for the 1.5 m/s inlet velocity. These figures clearly showed that at the same flowrate, the malfunctioning valve has these damaging eddies in a much larger area of space than the functioning valve, and the eddies are seen much farther downstream of the valve.

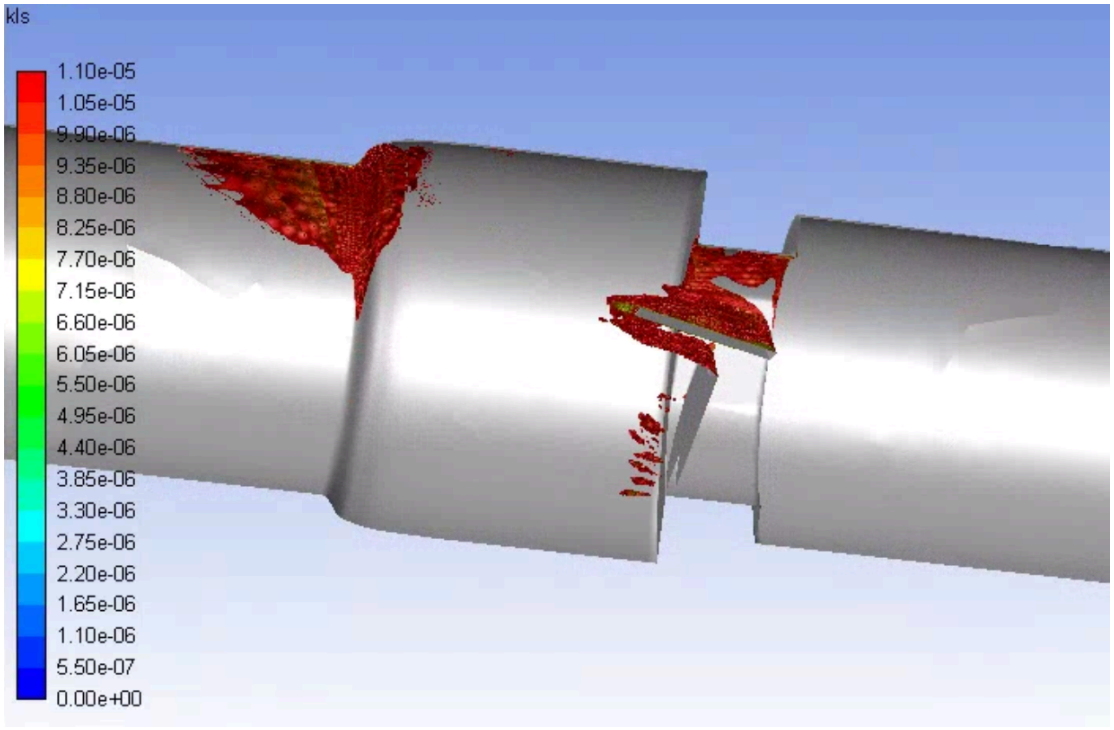

Figure 3.19 Volumetric contours of eddies with low KLS values (KLS ≤ 10 μm) for the malfunctioning valve with blood and an inlet velocity of 1.25 m/s (Note: The view is the inner portion of the valve, so the direction of the model appears reversed.)

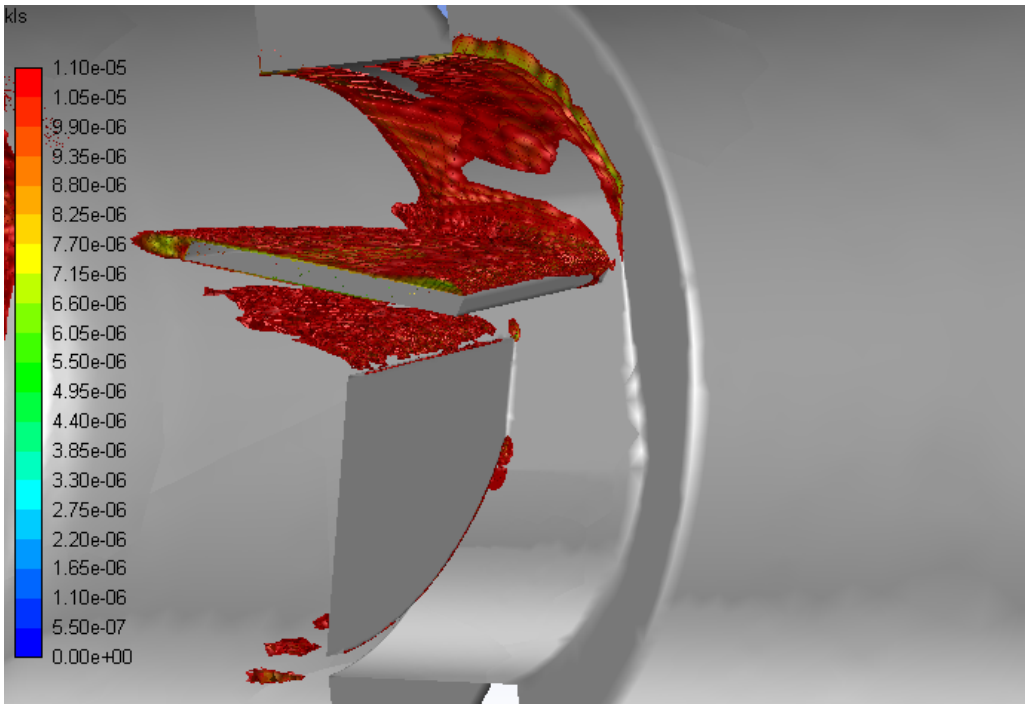

Figure 3.20 A close-up view of the volumetric contours of KLS values near the valve and leaflet in the malfunctioning valve (with blood and an inlet velocity = 1.25 m/s)

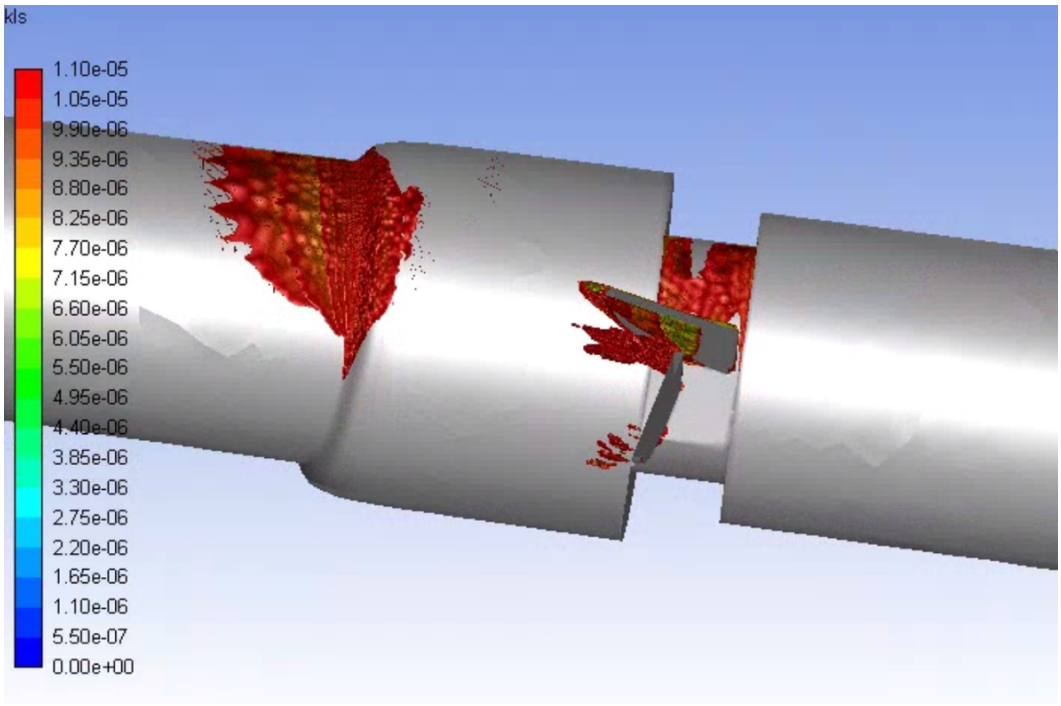

Figure 3.21 An alternate view of the volumetric contours of KLS values in the malfunctioning valve showing the underside of the working leaflet (with blood and an inlet velocity = 1.25 m/s)

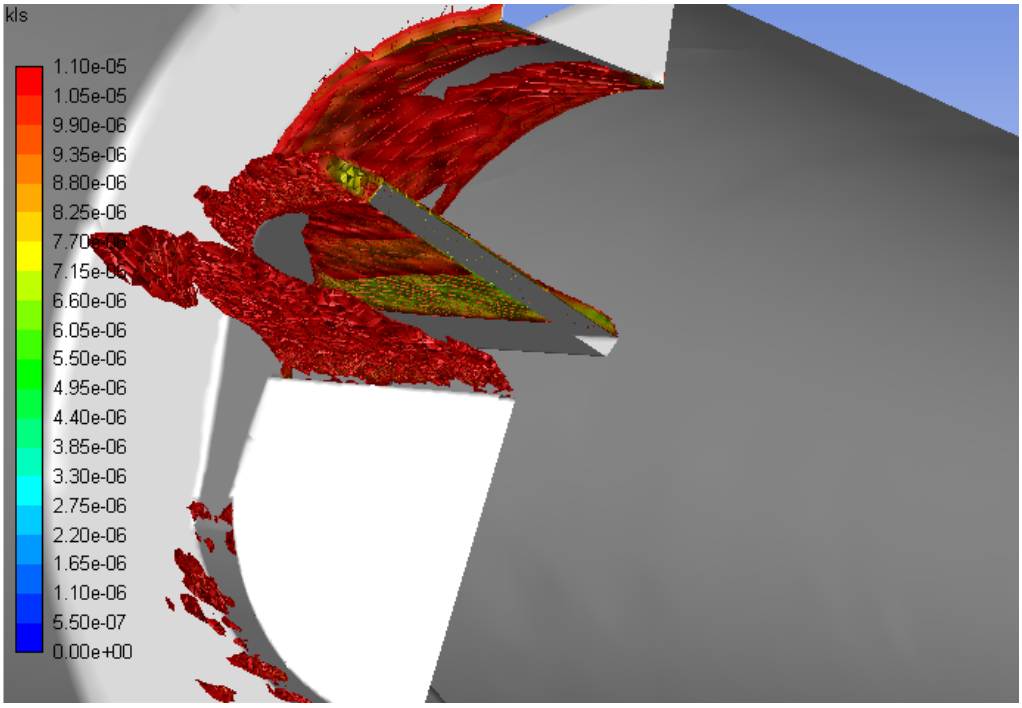

Figure 3.22 A close-up of the underside view of the volumetric contours of KLS values near the valve and leaflet in the malfunctioning valve (with blood and an inlet velocity = 1.25 m/s)

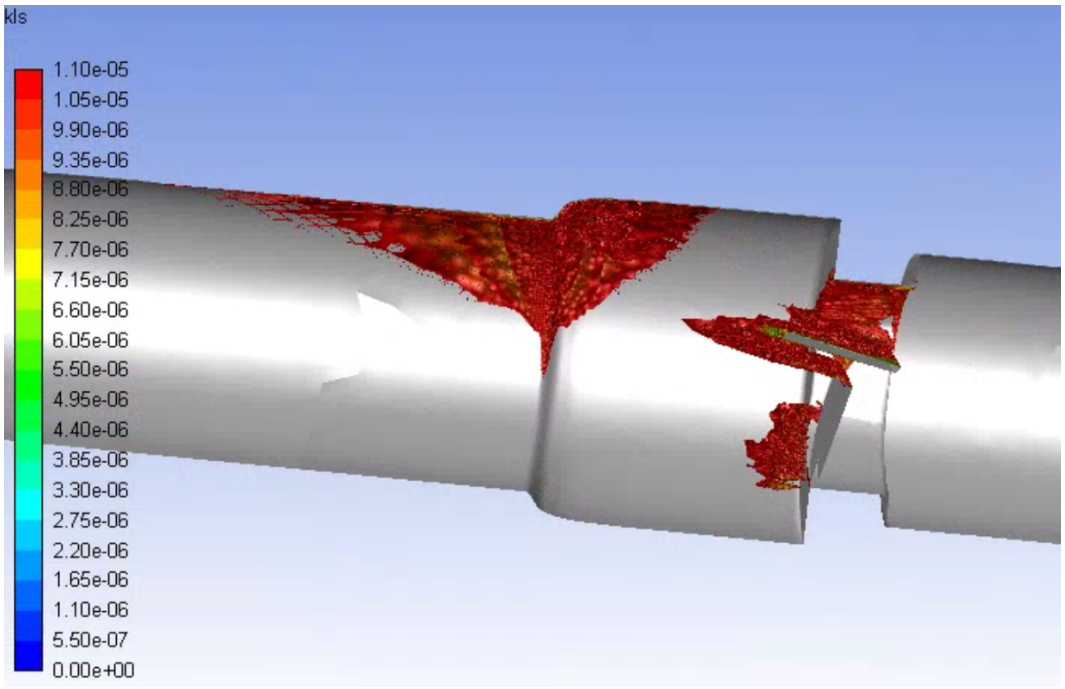

Figure 3.23 Volumetric contours of eddies with low KLS values (KLS ≤ 10 μm) for the malfunctioning valve with blood and an inlet velocity of 1.5 m/s (Note: The view is the inner portion of the valve, so the direction of the model appears reversed.)

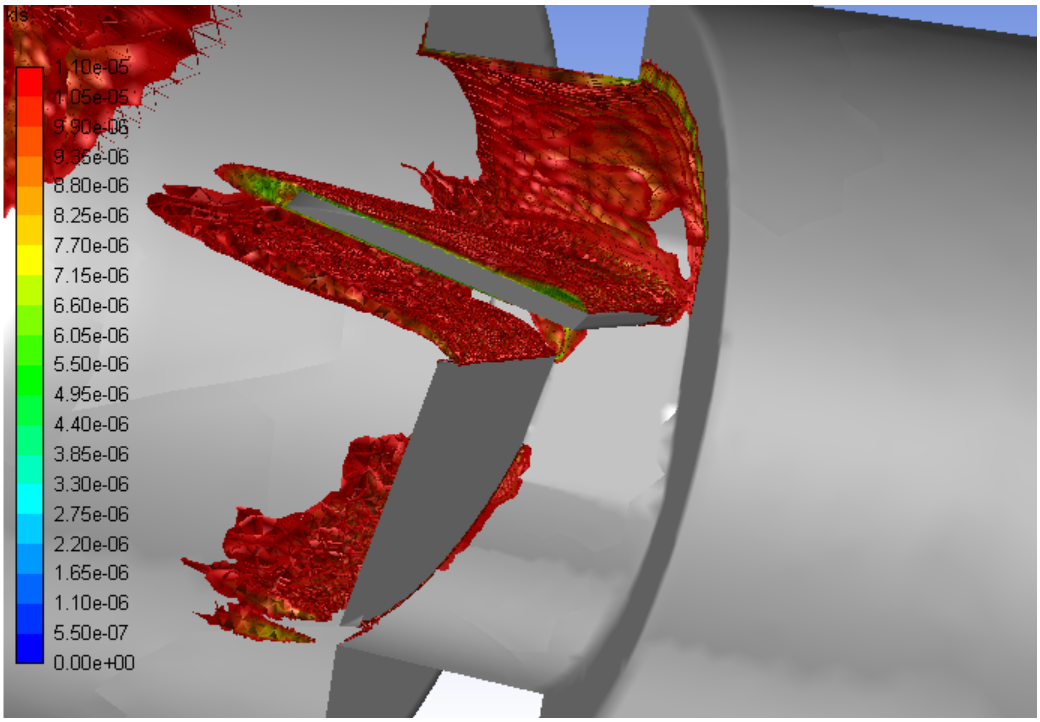

Figure 3.24 A close-up view of the volumetric contours of KLS values near the valve and leaflet in the malfunctioning valve (with blood and an inlet velocity = 1.5 m/s)

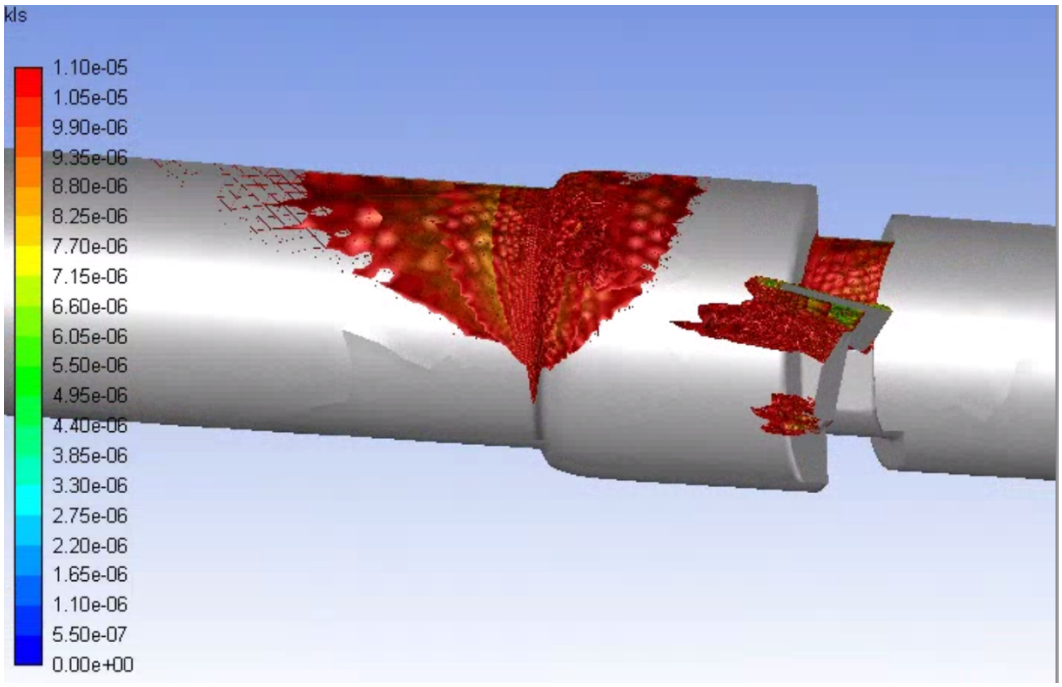

Figure 3.25 An alternate view of the volumetric contours of KLS values in the malfunctioning valve showing the underside of the working leaflet (with blood and an inlet velocity = 1.5 m/s)

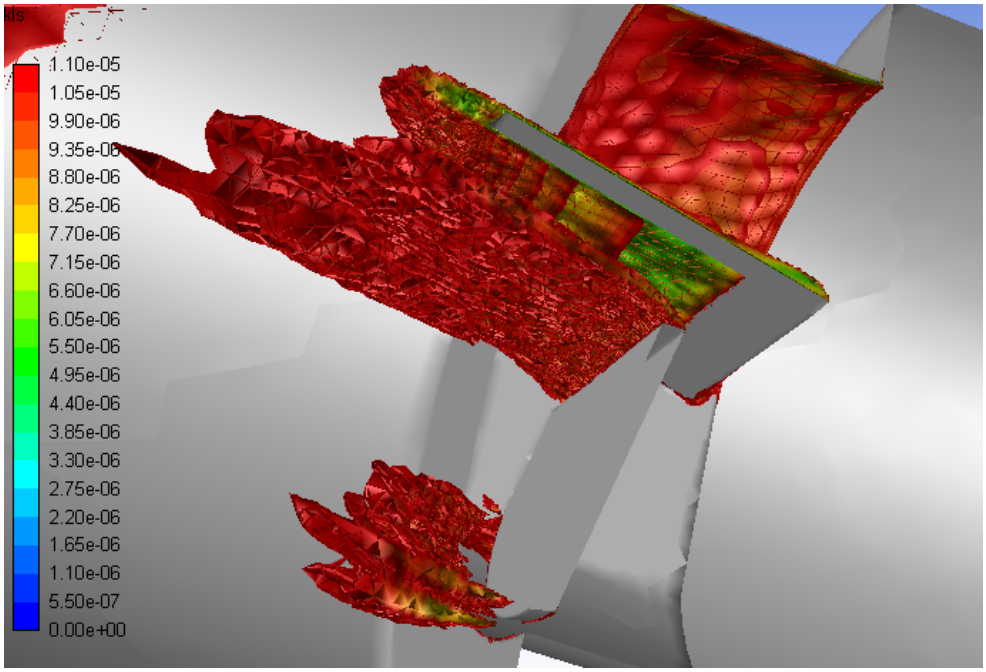

Figure 3.26 A close-up of the underside view of the volumetric contours of KLS values near the valve and leaflet in the malfunctioning valve (with blood and an inlet velocity = 1.5 m/s)

3.2.2 Distributions

The distribution of eddies (by both area and number) with a KLS of 10 μm or less were calculated for all of the runs. The distributions for the functioning valve model with an inlet velocity of 1.25 and 1.5 m/s were plotted in Figure 3.27 and Figure 3.28 respectively. The distribution data as well as the numbers and total surface areas of eddies from both runs are shown in Table 3.2 and Table 3.3.

The increase in velocity correlates to an increase in both the number of eddies (from 6.05×10^6 to 1.76×10^7) and total surface area of eddies (from 1.93×10^{-3} m^2 to 5.16×10^{-3} m^2) with a diameter equal to or less than 10 μm. There is also a decrease in the smallest eddy size (from 8 to 7 μm) and an increase in the percent of the smallest eddies with the increase in velocity. This is expected as an increase in velocity, increases the Reynolds number and turbulence of the flow, which increases the dissipation of energy and leads to decreased KLS values.

The total volume of regions where hemolysis is thought to occur is given for both valve types at both flowrates in Table 3.4. Depending on the equation used, this region could be the volume of space containing eddies with KLS ≤ 10 μm (Equation 1.3) or KLS ≤ 9 μm (Equation 1.4). For the functioning valve, an increase in flowrate correlates to an increase in the volumes of both KLS ranges, meaning an increase in the distribution of eddies and an increase in the regions where hemolysis occurs.

Table 3.2 Eddy number and surface area (SA) values and distributions for the functioning valve with an inlet velocity of 1.25 m/s

KLS (μm)	Number of Eddies	Percentage by Number (%)	Total SA of Eddies (m^2)	Percentage by SA (%)
8	2.73E+05	4.51	6.19E-05	3.20
9	2.09E+06	34.50	5.92E-04	30.64
10	3.69E+06	60.99	1.28E-03	66.16
Total	6.05E+06		1.93E-03	

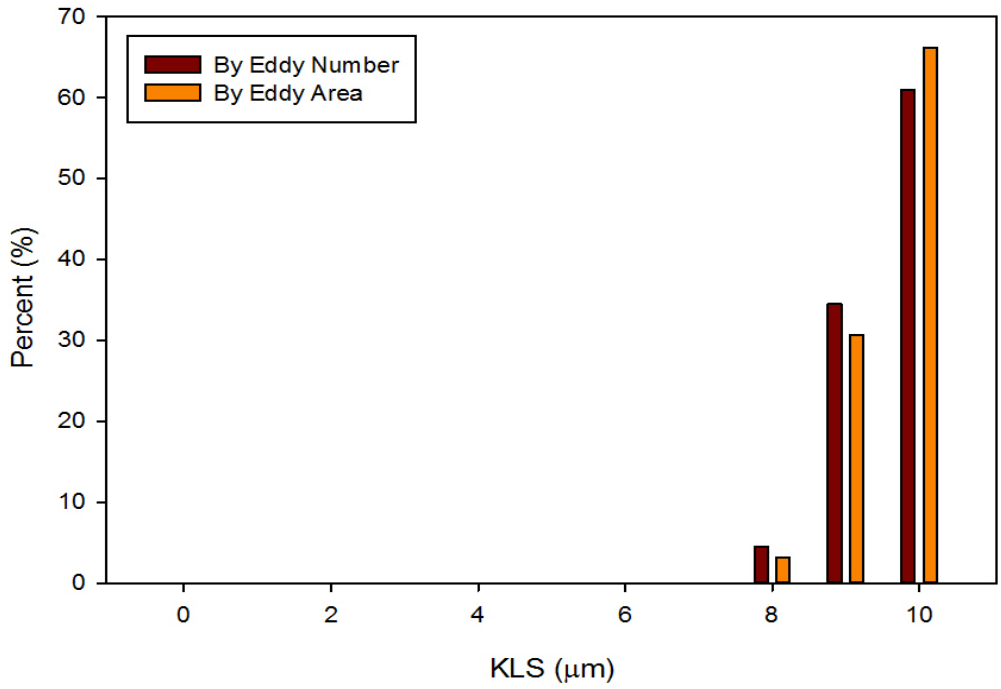

Figure 3.27 Distribution of eddy size by number and area for the functioning valve with an inlet velocity of 1.25 m/s

Table 3.3 Eddy number and surface area (SA) values and distributions for the functioning valve with an inlet velocity of 1.5 m/s

KLS (μm)	Number of Eddies	Percentage by Number (%)	Total SA of Eddies (m^2)	Percentage by SA (%)
7	4.75E+05	2.70	8.40E-05	1.63
8	4.14E+06	23.47	9.39E-04	18.21
9	5.96E+06	33.84	1.69E-03	32.80
10	7.05E+06	39.99	2.44E-03	47.35
Total	1.76E+07		5.16E-03	

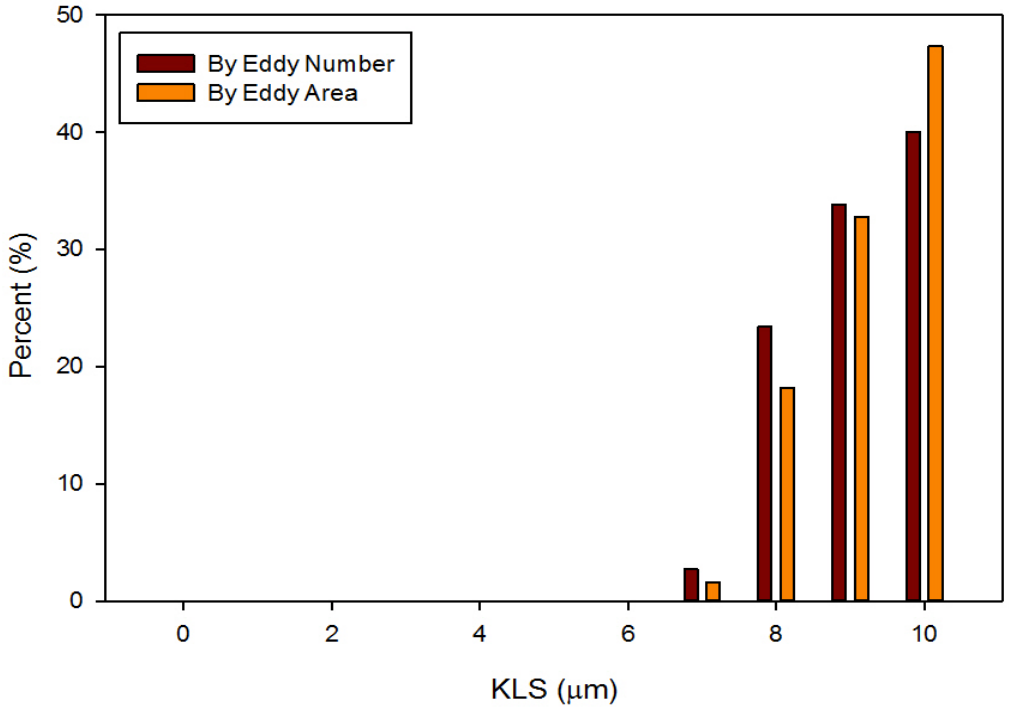

Figure 3.28 Distribution of eddy size by number and area for the functioning valve with an inlet velocity of 1.5 m/s

Table 3.4 Volumes of regions where hemolysis occurs

	Functioning Valve		**Malfunctioning Valve**	
	1.25 m/s	**1.5 m/s**	**1.25 m/s**	**1.5 m/s**
KLS ≤ 10 μm	3.260×10^{-9} m^3	8.385×10^{-9} m^3	1.174×10^{-7} m^3	4.044×10^{-7} m^3
KLS ≤ 9 μm	1.024×10^{-9} m^3	4.113×10^{-9} m^3	5.518×10^{-8} m^3	1.622×10^{-7} m^3

The distributions of eddies for the malfunctioning valve model were also plotted with inlet velocities of 1.25 and 1.5 m/s (Figure 3.29 and Figure 3.30). The eddy number, surface area, and distribution data for the malfunctioning valve model runs are given in Table 3.5 and Table 3.6. As was the case with the functioning valve, the increase in velocity correlates to an increase in both the number of eddies (from 2.73×10^8 to 9.09×10^8) and in total surface area of eddies (from 7.38×10^{-2} m^2 to 2.51×10^{-1} m^2) with a diameter equal to or less than 10 μm. Also like the functioning valve, the malfunctioning valve saw an increase in the percent of the smallest eddies and an increase in the volume where hemolysis occurs with the increase in velocity.

Table 3.5 Eddy number and surface area (SA) values and distributions for the malfunctioning valve with an inlet velocity of 1.25 m/s

KLS (μm)	Number of Eddies	Percentage by Number (%)	Total SA of Eddies (m^2)	Percentage by SA (%)
4	7.90E+03	2.90E-03	5.03E-07	6.81E-04
5	3.28E+06	1.20	3.11E-04	0.42
6	1.72E+07	6.32	2.29E-03	3.10
7	3.55E+07	13.01	6.27E-03	8.50
8	5.24E+07	19.19	1.19E-02	16.09
9	6.18E+07	22.65	1.75E-02	23.73
10	1.03E+08	37.63	3.56E-02	48.16
Total	2.73E+08		7.38E-02	

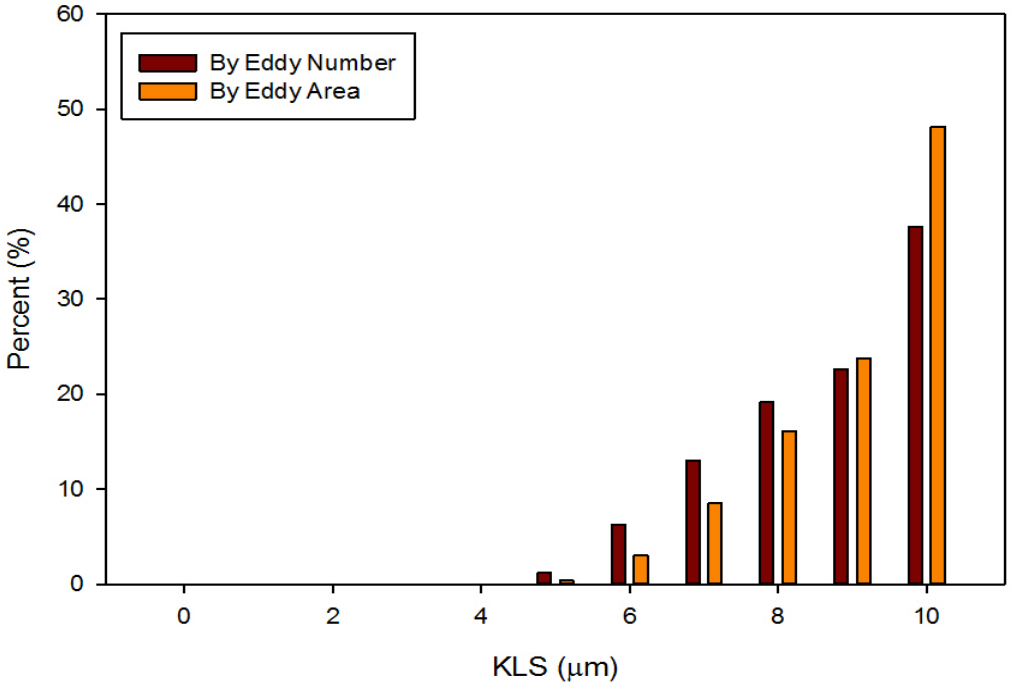

Figure 3.29 Distribution of eddy size by number and area for the malfunctioning valve with an inlet velocity of 1.25 m/s

Table 3.6 Eddy number and surface area (SA) values and distributions for the malfunctioning valve with an inlet velocity of 1.5 m/s

KLS (μm)	Number of Eddies	Percentage by Number (%)	Total SA of Eddies (m^2)	Percentage by SA (%)
4	2.05E+06	0.23	1.30E-04	0.052
5	3.16E+07	3.48	3.00E-03	1.20
6	6.40E+07	7.04	8.49E-03	3.38
7	8.93E+07	9.82	1.58E-02	6.29
8	1.12E+08	12.33	2.54E-02	10.14
9	2.10E+08	23.14	5.96E-02	23.77
10	4.00E+08	43.96	1.38E-01	55.17
Total	9.09E+08		2.51E-01	

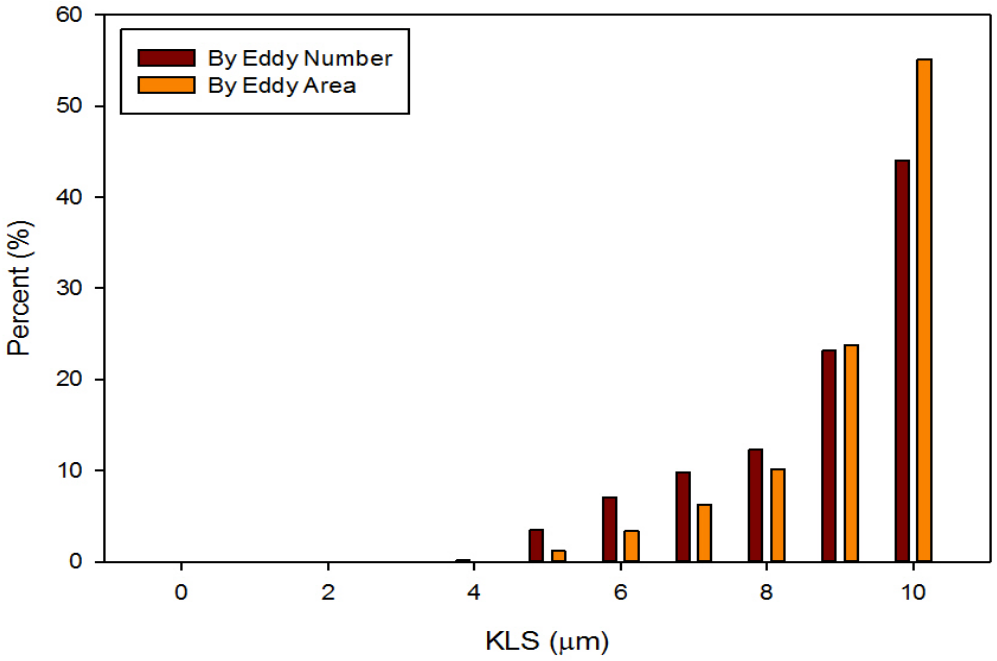

Figure 3.30 Distribution of eddy size by number and area for the malfunctioning valve with an inlet velocity of 1.5 m/s

In all cases, the largest percent of eddies both by area and number were the eddies in the range of 10 μm. When comparing the two valves at the same flowrate, the malfunctioning valve had eddies of smaller sizes (aka higher intensity) than the functioning valve. The number of eddies and the area taken up by eddies of all sizes were greater for the malfunctioning valve than for the functioning valve, meaning the totals for both of these values was also greater. Finally, the total distribution of eddies, or the total volume over which hemolysis occurs, was also greater for the malfunctioning valve than for the functioning valve.

3.3 Hemolysis Predictions

The hemolysis predictions based on the normalized surface areas of eddies were calculated using Equation 1.3 and Equation 1.4 (Table 3.7). These results show the hemolysis index per cubic meter (m^3) based on the regions with eddies with a diameter of 10 μm for Equation 1.3 and 9 μm for Equation 1.4. In all cases at the same flowrate, the malfunctioning valve had a higher expected hemolysis. In most cases, a higher flowrate also correlated to a higher expected hemolysis. This did not hold for Equation 1.3 for the malfunctioning valve.

This is because for a flowrate of 1.5 m/s there were a lot more eddies with an 8-10 μm diameter that took up a much larger volume down the length of the valve. When normalized, this would give a smaller hemolysis per m^3 when compared to the 1.25 m/s flowrate, which had a smaller volume to normalize all of the surface areas by. In other words, because the higher flowrate had a much larger percent of eddies of a larger size (lower intensity), at any point in the region of fluid that hemolysis is expected (region of

fluid with eddies with a KLS value of 10 μm or less), the hemolysis index on average would be lower than that of the lower flowrate.

Table 3.7 Normalized hemolysis predictions per m^3

	Functioning Valve		**Malfunctioning Valve**	
	1.25 m/s	**1.5 m/s**	**1.25 m/s**	**1.5 m/s**
Equation 1.3	0.675 %	0.716 %	0.833 %	0.818 %
Equation 1.4	1.097 %	1.135 %	1.273 %	1.314 %

To compare the total hemolysis expected in each case, the normalized hemolysis must be multiplied by the region containing hemolysis, or volume of space taken up by eddies of 10 μm (Equation 1.3) or 9 μm (Equation 1.4). These results are shown in Table 3.8. In all cases, a higher flowrate correlated with a higher total hemolysis index. At the same flowrate, the malfunctioning valve always had a higher predicted total hemolysis index than the functioning valve.

Table 3.8 Total hemolysis predictions

	Functioning Valve		**Malfunctioning Valve**	
	1.25 m/s	**1.5 m/s**	**1.25 m/s**	**1.5 m/s**
Equation 1.3	8.806×10^{-9} %	2.402×10^{-8} %	1.995×10^{-7} %	6.615×10^{-7} %
Equation 1.4	4.496×10^{-9} %	1.867×10^{-8} %	1.405×10^{-7} %	4.264×10^{-7} %

The hemolysis index can be calculated from blood as $HI = 100 * \frac{\Delta \mathrm{PH_b}}{H_b}$, where $\Delta \mathrm{PH_b}$ is the change in free plasma hemoglobin concentration, and H_b is the total hemoglobin concentration. Whole blood hemoglobin concentration ranges from 12.0-

16.0 g/dL for females to 13.5-17.5 g/dL for males[80]. From the total hemolysis predictions, the expected change in free plasma hemoglobin concentration can be calculated (Table 3.9 and Table 3.10). The results show that clinically there would be no discernible change seen in the concentration of free plasma hemoglobin after one pass through the heart valve. However, it is not unlikely that after multiple passes through the heart valve a higher change in free plasma hemoglobin would be detected.

Table 3.9 Change in free plasma hemoglobin after one pass through the artificial heart valves (for the lowest cited whole blood hemoglobin concentration 12.0 g/dL)

	Functioning Valve		**Malfunctioning Valve**	
	1.25 m/s	**1.5 m/s**	**1.25 m/s**	**1.5 m/s**
Equation 1.3	1.057×10^{-06}	2.882×10^{-06}	2.394×10^{-05}	7.938×10^{-05}
Equation 1.4	5.395×10^{-07}	2.240×10^{-06}	1.686×10^{-05}	5.1168×10^{-05}

Table 3.10 Change in free plasma hemoglobin after one pass through the artificial heart valves (for the highest cited whole blood hemoglobin concentration 17.5 g/dL)

	Functioning Valve		**Malfunctioning Valve**	
	1.25 m/s	**1.5 m/s**	**1.25 m/s**	**1.5 m/s**
Equation 1.3	1.541×10^{-06}	4.204×10^{-06}	3.491×10^{-05}	1.158×10^{-04}
Equation 1.4	7.868×10^{-07}	3.267×10^{-06}	2.459×10^{-05}	7.462×10^{-05}

4 Conclusions and Future Work

In this work a CFD three-dimensional model of a bileaflet artificial heart valve was created in both functioning and malfunctioning position. The results of simulations were compared with literature[68, 75, 76] to analyze the accuracy of the model. Velocity profiles and contours were also compared between the two valves. Additionally analysis was done on eddy intensity and distribution throughout the flow field, and the percent distribution of eddy sizes by both number of eddies and total surface area of eddies were compared between the valves at multiple flowrates. Finally, predictions of hemolysis were made using Equation 1.3 and Equation 1.4. The main conclusions found were:

1. The CFD model of the functioning valve gave good agreement with velocity data from literature using a medium mesh density and k-ω SST turbulence model with curvature and low-Re corrections. This validates the results of the heart valve models and gives confidence to other results obtained.
2. In the malfunctioning valve, increased velocity peaks were seen past the heart valve and leaflets near the fully open leaflet when compared to the closed leaflet or the functioning valve with two fully open leaflets. The closing of one leaflet forces more fluid flow around the working leaflet, increasing the velocity in that area.
3. This also caused a larger number of small eddies to form on the side of the valve and sinus near the functioning leaflet. Again, this is due to a larger amount of fluid flow in this region, creating more areas of turbulence and higher turbulent dissipation rates.

4. Results showed that an increased flowrate correlates with an increase of eddy intensity because of the increase in the number and areas of eddies of smaller sizes. It was also found that at the same flowrate, when compared to the functioning valve, the malfunctioning valve showed increased eddy intensity and eddies further down the flow field. This means that an increase in flowrate or a malfunction in the valve can increase both eddy intensity and distribution.
5. The predicted total hemolysis was higher at a higher flowrate for both valve types. At the same flowrate, the malfunctioning valve had a higher predicted total hemolysis. This comparative analysis shows that increased damage to erythrocytes can occur from an increase in flowrate, especially when caused by a malfunction in one of the leaflets.
6. The hemolysis predictions were lower than others in the literature [50, 51], though that may be due to the fact that only a single pass through the valve was analyzed in this research. These predictions support the view that current artificial heart valves do not cause a significant amount of hemolysis.

The lack of hemolytic damage may point to subhemolytic and sublethal damage being of greater concern than actual hemolysis for further improvement. Hemolysis and the equations can still be used as a comparative measure to determine which heart valves, flowrates, and malfunction types could be more damaging to the red blood cells. While these predictions support certain results, more in-vitro work may be necessary to directly compare the accuracy of the equations.

In-vitro data with indices of sublethal damage will be necessary to further improve artificial heart valves. Without data from actual heart valve experiments there

is no way to determine how well the models predict damage to cells. While comparing results with similar blood damage experiments, like VADs, can be helpful, the results are not as accurate.

More research should also be done to determine the sub hemolytic damage that occurs in RBCs. However, it is not easy to measure or characterize. Even though it is recognized as an issue, there are no good models to quantify it in ways that could be useful for comparison. For now, equations like the ones used in this research can predict what scenarios may be more or less damaging (based on predicted hemolysis) and can be used for design optimization.

References

1. Murphy, S.L., et al., *Deaths: Final data for 2015*, in *National Vital Statistics Reports*. 2017, National Center for Health Statistics: Hyattsville, MD.
2. Blackwell, D.L. and M.A. Villarroel, *Tables of Summary Health Statistics for U.S. Adults: 2016* in *National Health Interview Survey*. 2018, National Center for Health Statistics.
3. Association, A.H. *Roles of Your Four Heart Valves*. Sep 9, 2016 [cited 2018; Available from: http://www.heart.org/HEARTORG/Conditions/More/HeartValveProblemsandDisease/Roles-of-Your-Four-Heart-Valves_UCM_450344_Article.jsp#.W0J85dhKiu5.
4. Sigma-Aldrich. *Blood Basics*. [cited 2018; Available from: https://www.sigmaaldrich.com/life-science/metabolomics/enzyme-explorer/learning-center/plasma-blood-protein/blood-basics.html.
5. Association, A.H. *Heart Murmurs and Valve Disease*. Sep 26, 2016 [cited 2018; Available from: http://www.heart.org/HEARTORG/Conditions/More/HeartValveProblemsandDisease/Heart-Murmurs-and-Valve-Disease_UCM_450616_Article.jsp#.W0J8TNhKiu4.
6. Association, A.H. *Understanding Heart Valve Problems and Causes*. Jan 18, 2017 [cited 2018; Available from: http://www.heart.org/HEARTORG/Conditions/More/HeartValveProblemsandDisease/Understanding-Heart-Valve-Problems-and-Causes_UCM_450360_Article.jsp#.W0J8sdhKiu4.
7. Association, A.H. *Problem: Heart Valve Stenosis*. Oct 13, 2016 [cited 2018; Available from: http://www.heart.org/HEARTORG/Conditions/More/HeartValveProblemsandDisease/Problem-Heart-Valve-Stenosis_UCM_450369_Article.jsp#.W0J9c9hKiu5.
8. Association, A.H. *Problem: Aortic Valve Stenosis*. Sep 7, 2017 [cited 2018; Available from: http://www.heart.org/HEARTORG/Conditions/More/HeartValveProblemsandDisease/Problem-Aortic-Valve-Stenosis_UCM_450437_Article.jsp#.W0J9YdhKiu5.
9. Association, A.H. *Problem: Heart Valve Regurgitation*. Sep 29, 2016 [cited 2018; Available from: http://www.heart.org/HEARTORG/Conditions/More/HeartValveProblemsandDisease/Problem-Heart-Valve-Regurgitation_UCM_450736_Article.jsp#.W0J9UNhKiu5.
10. Association, A.H. *Problem: Mitral Valve Prolapse*. Dec 5, 2017 [cited 2018; Available from: http://www.heart.org/HEARTORG/Conditions/More/HeartValveProblemsandDisease/Problem-Mitral-Valve-Prolapse_UCM_450441_Article.jsp#.W0J9CthKiu5.

11. Association, A.H. *Single Ventricle Defects*. Sep 12, 2017 [cited 2018; Available from: http://www.heart.org/HEARTORG/Conditions/CongenitalHeartDefects/AboutCongenitalHeartDefects/Single-Ventricle-Defects_UCM_307037_Article.jsp#.W0J8-NhKiu5.
12. Association, A.H. *Understanding Your Heart Valve Treatment Options*. Jan 11, 2018 [cited 2018; Available from: http://www.heart.org/HEARTORG/Conditions/More/HeartValveProblemsandDisease/Understanding-Your-Heart-Valve-Treatment-Options_UCM_450784_Article.jsp#.W0KAJ9hKiu4.
13. Dasi, L.P., et al., *Fluid mechanics of artificial heart valves.* Clin Exp Pharmacol Physiol, 2009. **36**(2): p. 225-37.
14. Bloomfield, P., *Choice of heart valve prosthesis.* Heart, 2002. **87**(6): p. 583-589.
15. Hund, S.J., J.F. Antaki, and M. Massoudi, *On the representation of turbulent stresses for computing blood damage.* International Journal of Engineering Science, 2010. **48**(11): p. 1325-1331.
16. Antiga, L. and D.A. Steinman, *Rethinking turbulence in blood.* Biorheology, 2009. **46**(2): p. 77-81.
17. Aziz, A., et al., *The Cumulative and Sublethal Effects of Turbulence on Erythrocytes in a Stirred-Tank Model.* Annals of Biomedical Engineering, 2007. **35**(12): p. 2108-2120.
18. Kameneva, M.V., et al., *Effects of Turbulent Stresses upon Mechanical Hemolysis: Experimental and Computational Analysis.* ASAIO Journal, 2004. **50**(5).
19. Hill, M., *GUIDANCE ON TESTING FOR PAROXYSMAL NOCTURNAL HAEMOGLOBINURIA*. 2015, Heart of England NHS.
20. M. Sallam, A. and N. H.C. Hwang, *Human red blood cell hemolysis in a turbulent shear flow: Contribution of Reynolds shear stresses*. Vol. 21. 1984. 783-97.
21. Lu, P.C., H.C. Lai, and J.S. Liu, *A reevaluation and discussion on the threshold limit for hemolysis in a turbulent shear flow.* Journal of Biomechanics, 2001. **34**(10): p. 1361-1364.
22. Sutera, S.P. and M.H. Mehrjardi, *Deformation and fragmentation of human red blood cells in turbulent shear flow.* Biophysical Journal, 1975. **15**(1): p. 1-10.
23. Leverett, L.B., et al., *Red Blood Cell Damage by Shear Stress.* Biophysical Journal, 1972. **12**(3): p. 257-273.
24. Heuser, G. and R. Opitz, *A Couette viscometer for short time shearing of blood.* Biorheology. **17**: p. 17-24.
25. Paul, R., et al., *Shear Stress Related Blood Damage in Laminar Couette Flow.* Artificial Organs, 2003. **27**(6): p. 517-529.
26. Blackshear, P.L.J., F.D. Dorman, and J.H. Steinbach, *SOME MECHANICAL EFFECTS THAT INFLUENCE HEMOLYSIS.* ASAIO Journal, 1965. **11**(1): p. 112-117.
27. Giersiepen, M., et al., *Estimation of Shear Stress-related Blood Damage in Heart Valve Prostheses - in Vitro Comparison of 25 Aortic Valves.* The International Journal of Artificial Organs, 1990. **13**(5): p. 300-306.

28. Fraser, K.H., et al., *A Quantitative Comparison of Mechanical Blood Damage Parameters in Rotary Ventricular Assist Devices: Shear Stress, Exposure Time and Hemolysis Index.* Journal of Biomechanical Engineering, 2012. **134**(8): p. 0810021-08100211.
29. Zhang, T., et al., *Study of Flow-Induced Hemolysis Using Novel Couette-Type Blood-Shearing Devices.* Artificial Organs, 2011. **35**(12): p. 1180-1186.
30. Ding, J., et al., *Shear-Induced Hemolysis: Species Differences.* Artificial Organs, 2015. **39**(9): p. 795-802.
31. Arvand, A., M. Hormes, and H. Reul, *A Validated Computational Fluid Dynamics Model to Estimate Hemolysis in a Rotary Blood Pump.* Artificial Organs, 2005. **29**(7): p. 531-540.
32. Chan, W.K., et al., *Numerical Investigation of the Effect of Blade Geometry on Blood Trauma in a Centrifugal Blood Pump.* Artificial Organs, 2002. **26**(9): p. 785-793.
33. Song, X., et al., *Computational Fluid Dynamics Prediction of Blood Damage in a Centrifugal Pump.* Artificial Organs, 2003. **27**(10): p. 938-941.
34. Arora, D., M. Behr, and M. Pasquali, *A Tensor-based Measure for Estimating Blood Damage.* Artificial Organs, 2004. **28**(11): p. 1002-1015.
35. Vitale, F., et al., *A multiscale, biophysical model of flow-induced red blood cell damage.* AIChE Journal, 2013. **60**(4): p. 1509-1516.
36. Taskin, M.E., et al., *Evaluation of Eulerian and Lagrangian Models for Hemolysis Estimation.* ASAIO Journal, 2012. **58**(4).
37. Stein, P.D. and H.N. Sabbah, *Turbulent blood flow in the ascending aorta of humans with normal and diseased aortic valves.* Circulation Research, 1976. **39**(1): p. 58.
38. Sabbah, H.N. and P.D. Stein, *Turbulent blood flow in humans: its primary role in the production of ejection murmurs.* Circulation Research, 1976. **38**(6): p. 513.
39. Jones, S.A., *A relationship between reynolds stresses and viscous dissipation: Implications to red cell damage.* Annals of Biomedical Engineering, 1995. **23**(1): p. 21-28.
40. Yen, J.-H., et al., *The effect of turbulent viscous shear stress on red blood cell hemolysis.* Journal of Artificial Organs, 2014. **17**(2): p. 178-185.
41. Lee, H., E. Tatsumi, and Y. Taenaka, *Experimental Study on the Reynolds and Viscous Shear Stress of Bileaflet Mechanical Heart Valves in a Pneumatic Ventricular Assist Device.* ASAIO Journal, 2009. **55**(4).
42. Ozturk, M., A.E. O'Rear, and V.D. Papavassiliou, *Reynolds Stresses and Hemolysis in Turbulent Flow Examined by Threshold Analysis.* Fluids, 2016. **1**(4).
43. Yacoub, M.H. and D.H. Keeling, *Chronic haemolysis following insertion of ball valve prostheses.* British Heart Journal, 1968. **30**(5): p. 676-678.
44. Kloster, F.E., *Diagnosis and management of complications of prosthetic heart valves.* The American Journal of Cardiology, 1975. **35**(6): p. 872-885.
45. Rajiv, M., et al., *Evaluation of hemolysis in patients with prosthetic heart valves.* Clinical Cardiology, 1998. **21**(6): p. 387-392.

46. Amidon, T.M., et al., *Mitral and aortic paravalvular leaks with hemolytic anemia.* American Heart Journal, 1993. **125**(1): p. 266-268.
47. Mecozzi, G., et al., *Intravascular hemolysis in patients with new-generation prosthetic heart valves: A prospective study.* The Journal of Thoracic and Cardiovascular Surgery, 2002. **123**(3): p. 550-556.
48. Shivakumaraswamy, T., et al., *Intravascular hemolysis in patients with normally functioning mechanical heart valves in mitral position.* Indian Journal of Thoracic and Cardiovascular Surgery, 2006. **22**(4): p. 215-218.
49. Sabzi, F. and D. Khosravi, *Hemolytic Anemia after Aortic Valve Replacement: a Case Report.* Acta Medica Iranica; Vol 53, No 9 (2015), 2015.
50. Susin, F.M., et al., *Integrated strategy for in vitro characterization of a bileaflet mechanical aortic valve.* BioMedical Engineering OnLine, 2017. **16**: p. 29.
51. de Tullio, M.D., et al., *Computational prediction of mechanical hemolysis in aortic valved prostheses.* European Journal of Mechanics - B/Fluids, 2012. **35**: p. 47-53.
52. Toninato, R., G. Fadda, and F. Susin, *A Red Blood Cell Model to Estimate the Hemolysis Fingerprint of Cardiovascular Devices: A RED BLOOD CELL MODEL FOR HEMOLYSIS.* Vol. 42. 2017.
53. Yin, W., E.C. Ngwe, and D.A. Rubenstein, *A Biocompatible Flow Chamber to Study the Hemodynamic Performance of Prosthetic Heart Valves.* ASAIO Journal, 2012. **58**(5).
54. Linde, T., et al., *Aortic Root Compliance Influences Hemolysis in Mechanical Heart Valve Prostheses: An In-Vitro Study.* The International Journal of Artificial Organs, 2012. **35**(7): p. 495-502.
55. Ko, T.-Y., et al., *Frequency and Significance of Intravascular Hemolysis Before and After Transcatheter Aortic Valve Implantation in Patients With Severe Aortic Stenosis.* The American Journal of Cardiology, 2018. **121**(1): p. 69-72.
56. Cho, I.J., et al., *Different Clinical Outcome of Paravalvular Leakage After Aortic or Mitral Valve Replacement.* The American Journal of Cardiology, 2011. **107**(2): p. 280-284.
57. Hwang, H.Y., et al., *Paravalvular Leak After Mitral Valve Replacement: 20-Year Follow-Up.* The Annals of Thoracic Surgery, 2015. **100**(4): p. 1347-1352.
58. Quinlan, N.J. and P.N. Dooley, *Models of Flow-Induced Loading on Blood Cells in Laminar and Turbulent Flow, with Application to Cardiovascular Device Flow.* Annals of Biomedical Engineering, 2007. **35**(8): p. 1347-1356.
59. Liu, J.S., P.C. Lu, and S.H. Chu, *Turbulence Characteristics Downstream of Bileaflet Aortic Valve Prostheses.* Journal of Biomechanical Engineering, 1999. **122**(2): p. 118-124.
60. Dooley, P.N. and N.J. Quinlan, *Effect of Eddy Length Scale on Mechanical Loading of Blood Cells in Turbulent Flow.* Annals of Biomedical Engineering, 2009. **37**(12): p. 2449.
61. Ozturk, M., A. O'Rear Edgar, and V. Papavassiliou Dimitrios, *Hemolysis Related to Turbulent Eddy Size Distributions Using Comparisons of Experiments to Computations.* Artificial Organs, 2015. **39**(12): p. E227-E239.

62. Ozturk, M., D.V. Papavassiliou, and E.A. O'Rear, *An Approach for Assessing Turbulent Flow Damage to Blood in Medical Devices.* Journal of Biomechanical Engineering, 2016. **139**(1): p. 011008-011008-8.
63. Forstrom, R.J., *A New Measure of Erythrocyte Membrane Strength—The Jet Fragility Test*. 1969, University of Minnesota,: Minneapolis, MN.
64. Khalili, F., *Hemodynamics of a Bileaflet Mechanical Heart Valve with Different Levels of Dysfunction*. Vol. 2. 2017.
65. Smadi, O., et al., *Flow through a defective mechanical heart valve: A steady flow analysis.* Medical Engineering & Physics, 2009. **31**(3): p. 295-305.
66. Smadi, O., et al., *Numerical and experimental investigations of pulsatile blood flow pattern through a dysfunctional mechanical heart valve.* Journal of Biomechanics, 2010. **43**(8): p. 1565-1572.
67. Raghav, V., S. Sastry, and N. Saikrishnan, *Experimental Assessment of Flow Fields Associated with Heart Valve Prostheses Using Particle Image Velocimetry (PIV): Recommendations for Best Practices.* Cardiovasc Eng Technol, 2018.
68. Hutchinson, C., *Stereoscopic PIV In Steady Flow Through a Bileaflet Mechanical Heart Valve*, in *Mechanical and Industrial Engineering*. 2009, University of Toronto.
69. *CARBOMEDICS STANDARD AORTIC VALVE*. LisaNova.
70. Ge, L., et al., *Characterization of Hemodynamic Forces Induced by Mechanical Heart Valves: Reynolds vs. Viscous Stresses.* Annals of Biomedical Engineering, 2008. **36**(2): p. 276-297.
71. Ge, L., et al., *Flow in a Mechanical Bileaflet Heart Valve at Laminar and Near-Peak Systole Flow Rates: CFD Simulations and Experiments.* Journal of Biomechanical Engineering, 2005. **127**(5): p. 782-797.
72. Stevenson, D.M. and A.P. Yoganathan, *Numerical simulation of steady turbulent flow through trileaflet aortic heart valves—I. Computational scheme and methodology.* Journal of Biomechanics, 1985. **18**(12): p. 899-907.
73. Xu, J., et al. *Simulation of Bileaf Curved Surface Mechanical Heart Valve: A Steady Flow Analysis*. in *2010 4th International Conference on Bioinformatics and Biomedical Engineering*. 2010.
74. Kim, S.H., K.B. Chandran, and C.J. Chen, *Numerical Simulation of Steady Flow in a Two-Dimensional Total Artificial Heart Model.* Journal of Biomechanical Engineering, 1992. **114**(4): p. 497-503.
75. Blackmore, A. and S. Pierre, *LARGE EDDY SIMULATIONS AND PARTICLE IMAGE VELOCIMETRY EXPERIMENTS WITHIN A BIMHV FLOW NEAR PEAK SYSTOLE*, in *International Symposium on Turbulence and Shear Flow Phenomena* 2013: Poitiers, France.
76. Hutchison, C., P. Sullivan, and C.R. Ethier, *Measurements of steady flow through a bileaflet mechanical heart valve using stereoscopic PIV.* Medical & Biological Engineering & Computing, 2011. **49**(3): p. 325-335.
77. Jahandardoost, M., G. Fradet, and H. Mohammadi, *Effect of heart rate on the hemodynamics of bileaflet mechanical heart valves' prostheses (St. Jude Medical) in the aortic position and in the opening phase: A computational study.*

Proceedings of the Institution of Mechanical Engineers, Part H: Journal of Engineering in Medicine, 2016. **230**(3): p. 175-190.
78. Pan, W., B. Caswell, and G.E. Karniadakis, *A low-dimensional model for the red blood cell.* Soft matter, 2010. **6**(18): p. 10.1039/C0SM00183J.
79. Bagchi, P., *Mesoscale Simulation of Blood Flow in Small Vessels.* Biophysical Journal, 2007. **92**(6): p. 1858-1877.
80. Cabot, R.C., et al., *Laboratory Reference Values.* The New England Journal of Medicine, 2004. **351**(15): p. 1548-1563.

Appendices

Appendix A: Additional Heart Valve Schematics

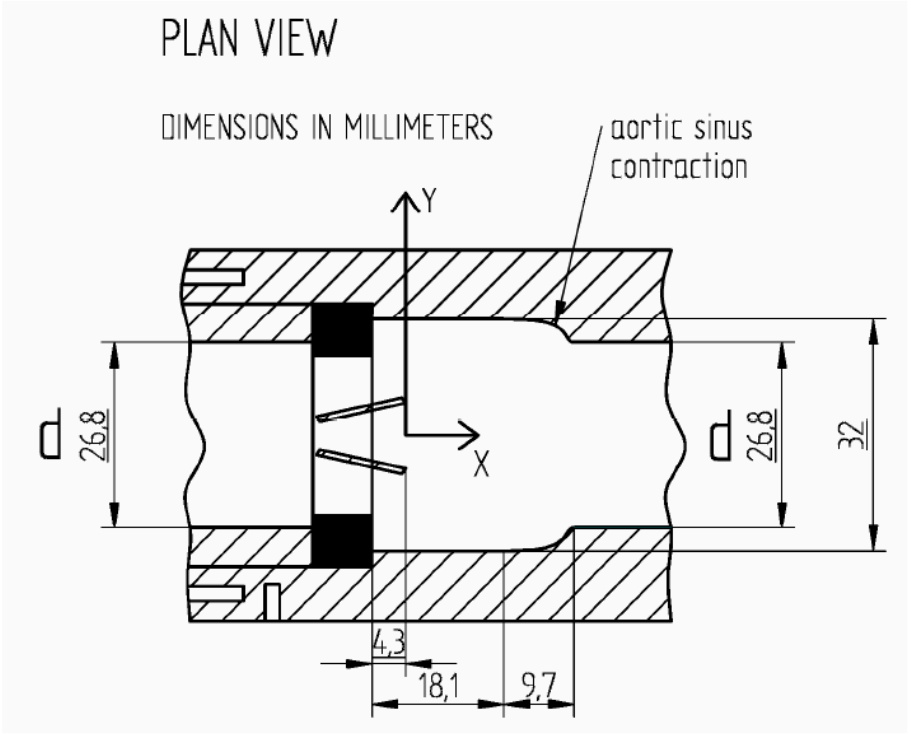

Figure 0.1 Schematic of valve system[68]

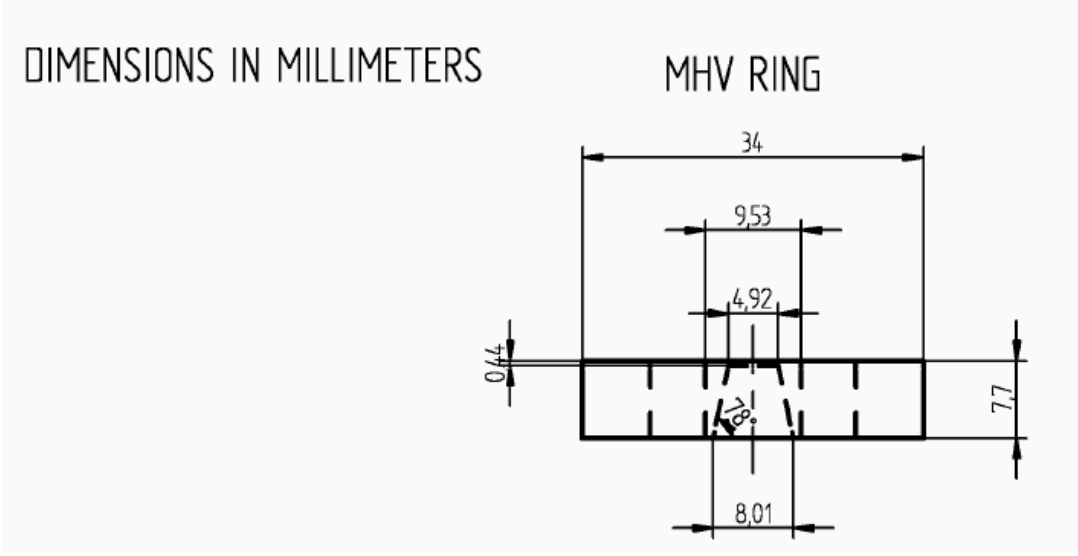

Figure 0.2 Schematic of valve frame and leaflets[68]

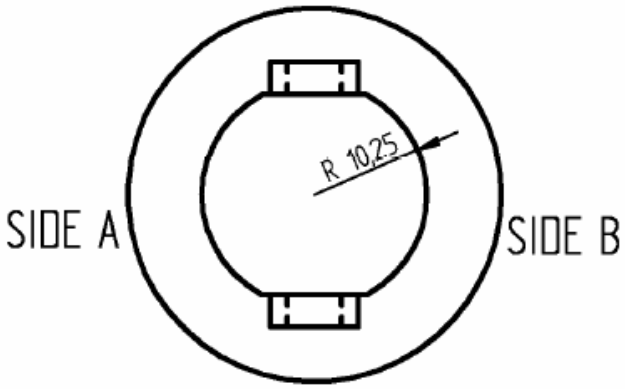

Figure 0.3 Diagram of valve frame radius[68]

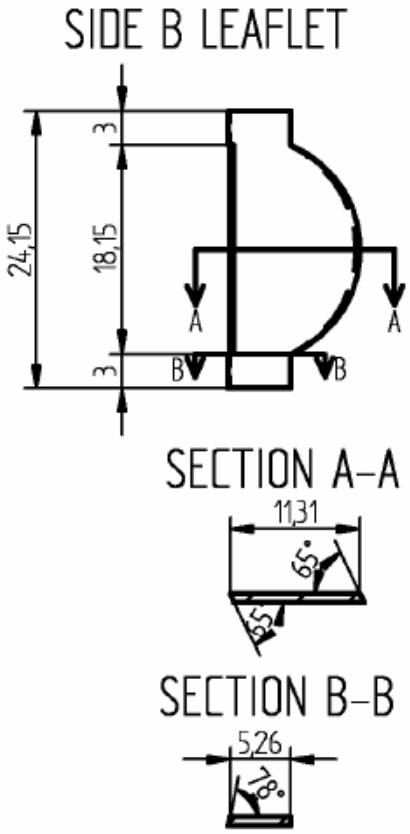

Figure 0.4 Diagram of leaflet dimensions[68]

Appendix B: Eddy Analysis Process

Because Fluent does not automatically calculate the Kolmogorov length scale (KLS), it must be defined as a custom field function within Fluent. To do this in Fluent 18.1, select the 'User Defined' tab on the top and under 'Field Functions' select 'Custom.' This pulls up a key pad, where the formula for KLS was defined (Equation 0.1), using viscosity (μ), density (ρ), and the turbulent dissipation rate (ε) (Figure 0.5). The turbulent dissipation rate must be selected from the operational field functions. All examples in this section come from the simulation of the functioning valve with blood and an inlet flowrate of 1.5 m/s.

$$KLS = \left(\frac{\nu^3}{\epsilon}\right)^{\frac{1}{4}} = \left(\frac{\mu^3}{\rho^3\epsilon}\right)^{\frac{1}{4}} \qquad \textbf{Equation 0.1}$$

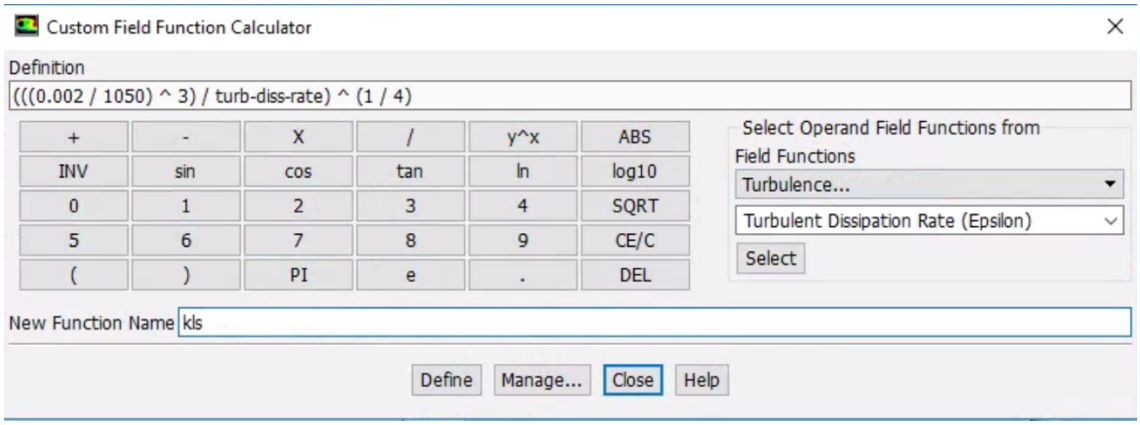

Figure 0.5 Defining KLS as a custom field function in Fluent

This definition step can be done before or after the calculations for the simulations are run. The rest of the process must be done after the calculations are considered complete. The next step is to create surfaces down the length of the flow field. Under the 'Setting Up Domain' tab on the top and under 'Surface' select 'Create'

and ‘Plane.’ From here, a plane can be created from three points anywhere within the flow field, as shown for x=400 mm downstream (Figure 0.6). In this research, planes were created 0.5 mm apart for the entire region containing eddy sizes of interest.

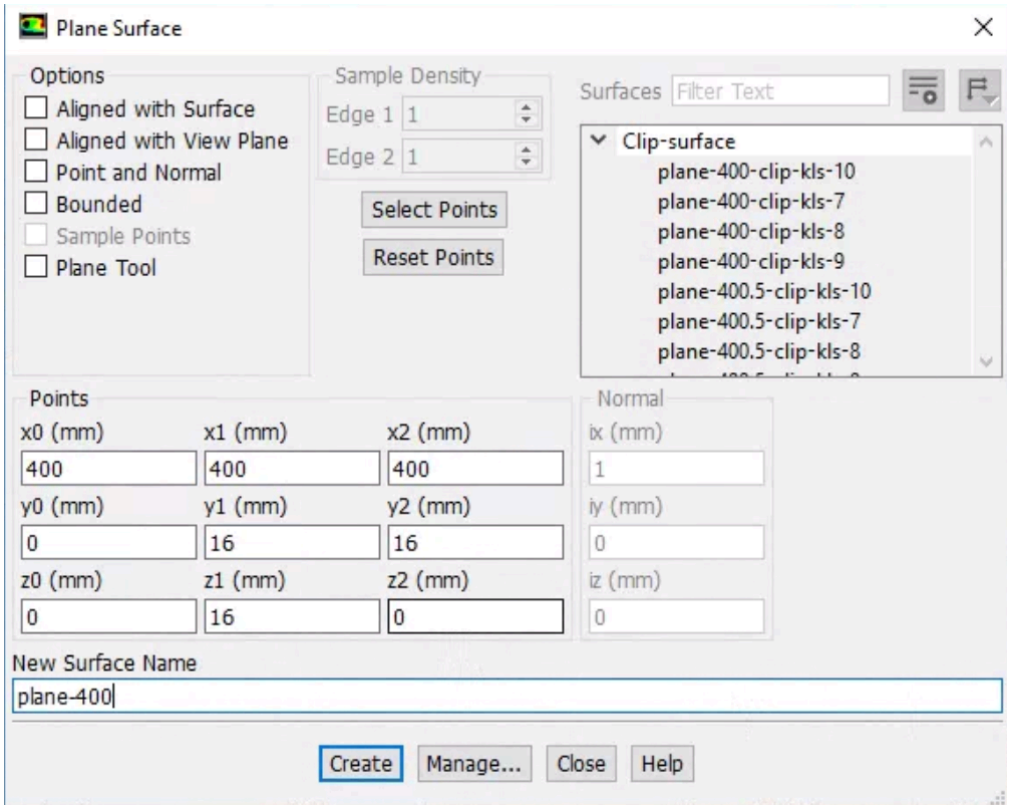

Figure 0.6 Example of making a plane (x=400 mm downstream)

Once the planes are created, they can be clipped into smaller planes with eddy sizes of 1 μm units. These are called iso-clips and are selected from the same location as plane creation. From the selection screen, a plane must be chosen (in this calse plane-400) and clipped to values of ‘Custom Field Functions’ and ‘kls.’ When the ‘Compute’ button is clicked, the minimum and maximum KLS values will be calculated on the selected plane (Figure 0.7). Iso-clips are then created in 1 μm increments

starting from the smallest size in the eddy field, which in the example would be 7 to 8 μm (Figure 0.8). This is continued for all planes created in the flow field until the minimum KLS value is too small.

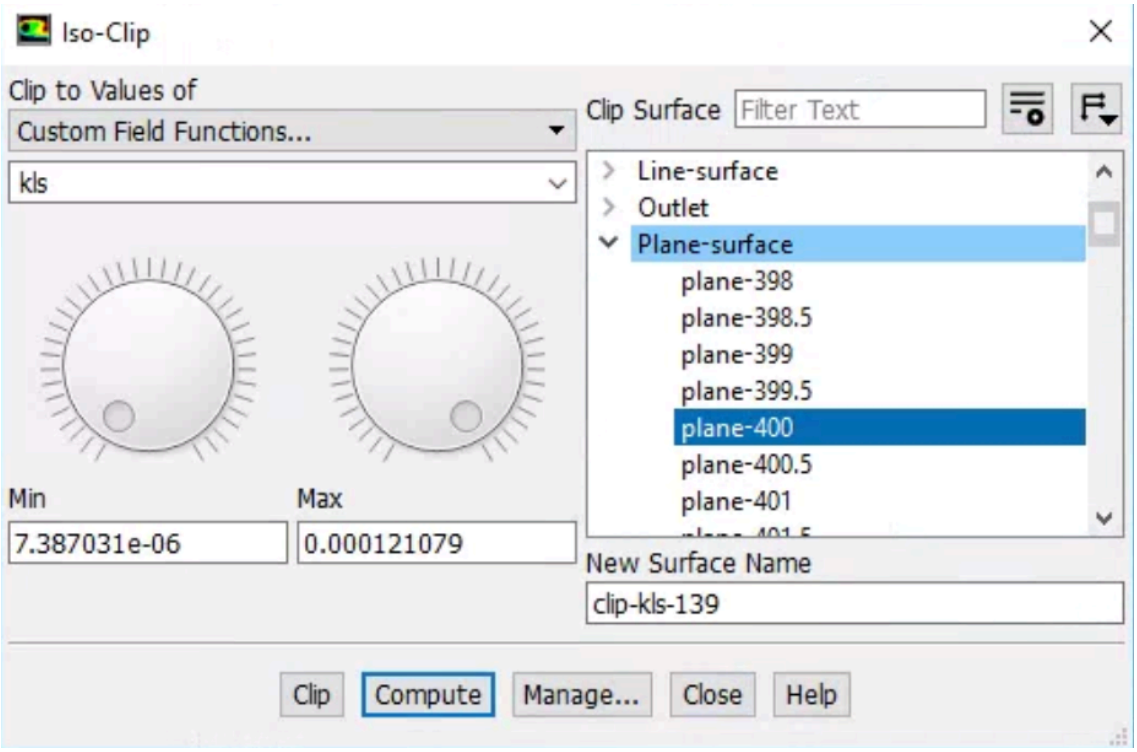

Figure 0.7 Example for calculating the KLS range on a plane

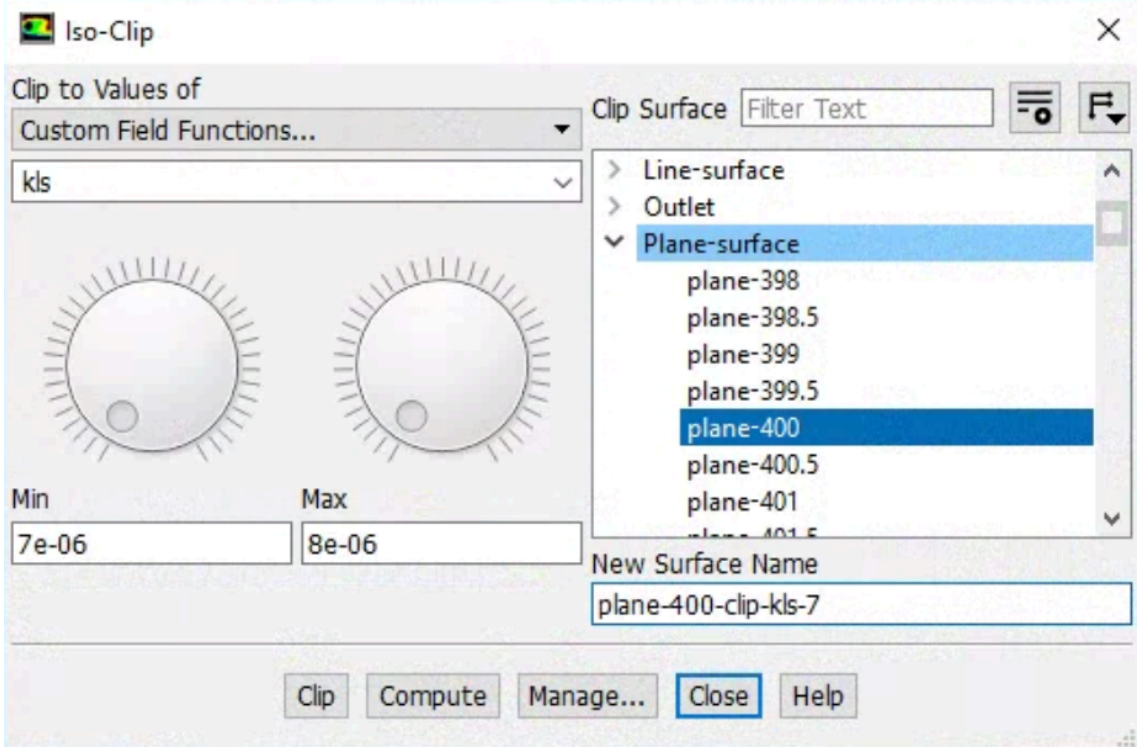

Figure 0.8 Example of creating an iso-clip

Once all iso-clips are created, the area of each iso-clip must be created. This is done under the 'Results' tab on the lef-hand side under 'Reports' and 'Surface Integral.' The report type selected should be 'Area' and the 'Field Variable' should be automatically filled to 'Custom Field Functions' and 'kls' (Figure 0.9). All clip-surfaces are selected and then written to a comma-separated values (CSV) file, which can be opened with excel. The area of each iso-clip will be listed next to its name, along with the total area of all iso-clips selected.

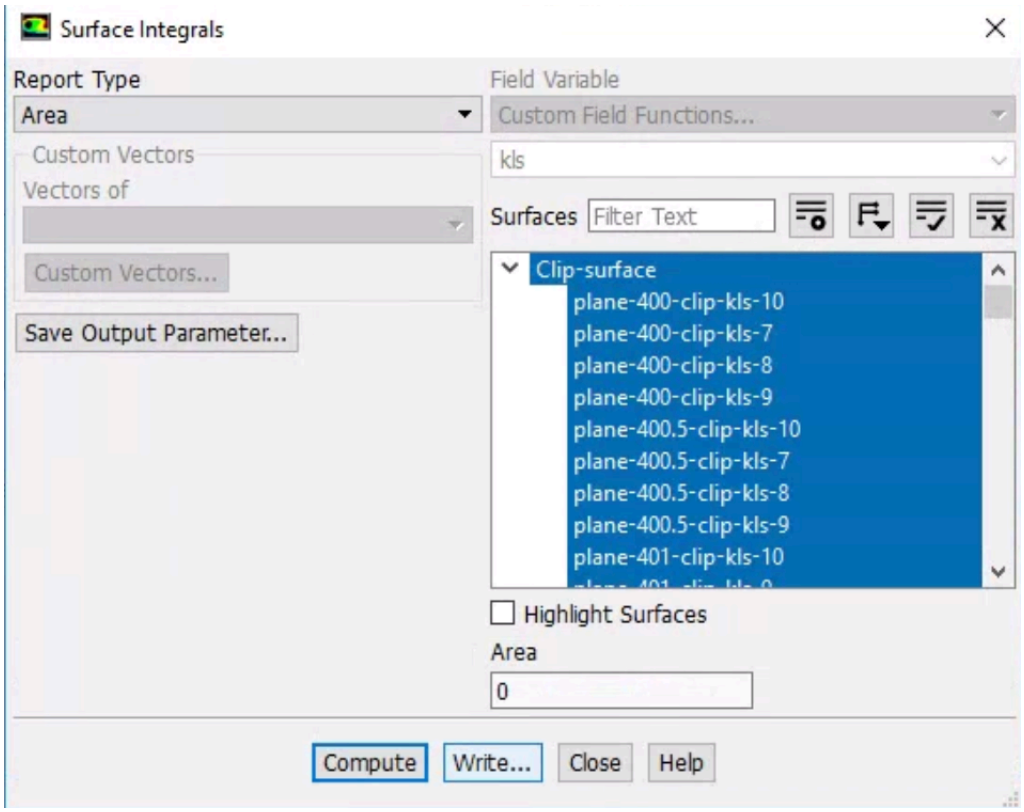

Figure 0.9 Example of how to calculate the area of the iso-clips

All of this information is organized in an excel spreadsheet where calculations of eddy distribution and hemolysis can be done (Figure 0.10). In this example, column A lists the iso-clip name, column B lists the area of that clip, and column C lists the KLS size in meters. This gives the area made up by eddies of any each size range at that point in the flow. Then in column D, the area of eddies of that range are averaged between the selected plane and the next plane in the region of flow. For example, the area of the iso-clip from 7 to 8 μm for the plane 400 mm into the flow is averaged with the same clip 400.5 mm into the flow. This average can then be multiplied by the distance between the planes (0.5 mm) to get the approximate volume of space taken up by eddies of that size range, as is done in column E (Equation 0.2).

The diameter of the eddies in column F are calculated as the average of the KLS size range of the clip. So, for 7 to 8 μm, 7.5 μm would be used as the diameter of the eddies. Using this diameter, in column G, the volume of one eddy of that size can be calculated (Equation 0.3). Then column H calculates the total number of eddies in that space by dividing the volume those eddies make-up by the volume of one eddy of that size (Equation 0.4). Finally, the surface area of one eddy of that size is calculated in column I (Equation 0.5). These are the area of interest, as this is where damage to red blood cells (RBCs) is likely to occur. So the surface areas can summed and used for the hemolysis equations. The areas and numbers of eddies of each size can also be summed for the entire flow field to find the distributions.

$$\mathrm{V_{total}} = \mathrm{A_{avg}} * d_{between\ planes} = \mathrm{A_{avg}} * 0.5\ mm \qquad \textbf{Equation 0.2}$$

$$V_{eddy} = \frac{4}{3}\pi\left(\frac{KLS}{2}\right)^3 \qquad \textbf{Equation 0.3}$$

$$\mathrm{N_{eddy}} = \frac{V_{total}}{V_{eddy}} \qquad \textbf{Equation 0.4}$$

$$A_{eddy} = N_{eddy} * 4\pi\left(\frac{KLS}{2}\right)^2 \qquad \textbf{Equation 0.5}$$

	A	B	C	D	E	F	G	H	I
1		**Area (m2)**	kls (m)	Average Area (m^2)	Volume (m^3)	diameter (m)	Eddy Volume (m^3)	Eddy #	Eddy Area (m^2)
2	**plane 399.5**	exported			Equation 0.2		Equation 0.3	Equation 0.4	Equation 0.5
3	**plane 400**		0						
4	clip-plane-400-kls-0		0.000001	0	0	0.0000005	6.54498E-20	0	0
5	clip-plane-400-kls-1		0.000002	0	0	0.0000015	1.76715E-18	0	0
6	clip-plane-400-kls-2		0.000003	0	0	0.0000025	8.18123E-18	0	0
7	clip-plane-400-kls-3		0.000004	0	0	0.0000035	2.24493E-17	0	0
8	clip-plane-400-kls-4		0.000005	0	0	0.0000045	4.77129E-17	0	0
9	clip-plane-400-kls-5		0.000006	0	0	0.0000055	8.71137E-17	0	0
10	clip-plane-400-kls-6		0.000007	0	0	0.0000065	1.43793E-16	0	0
11	clip-plane-400-kls-7	2.92E-08	0.000008	2.00828E-08	1.00414E-11	0.0000075	2.20893E-16	45458.08101	8.03311E-06
12	clip-plane-400-kls-8	2.70E-07	0.000009	1.4986E-07	7.49298E-11	0.0000085	3.21555E-16	233023.1963	5.28916E-05
13	clip-plane-400-kls-9	2.18E-07	0.00001	1.30933E-07	6.54665E-11	0.0000095	4.48921E-16	145830.9032	4.13473E-05
14	clip-plane-400-kls-10	3.35E-07	0.000011	2.07137E-07	1.03569E-10	0.0000105	6.06131E-16	170868.36	5.91821E-05
15	**plane 400.5**		0						
16	clip-plane-400.5-kls-0		0.000001	0	0	0.0000005	6.54498E-20	0	0
17	clip-plane-400.5-kls-1		0.000002	0	0	0.0000015	1.76715E-18	0	0
18	clip-plane-400.5-kls-2		0.000003	0	0	0.0000025	8.18123E-18	0	0
19	clip-plane-400.5-kls-3		0.000004	0	0	0.0000035	2.24493E-17	0	0
20	clip-plane-400.5-kls-4		0.000005	0	0	0.0000045	4.77129E-17	0	0
21	clip-plane-400.5-kls-5		0.000006	0	0	0.0000055	8.71137E-17	0	0
22	clip-plane-400.5-kls-6		0.000007	0	0	0.0000065	1.43793E-16	0	0
23	clip-plane-400.5-kls-7	1.10E-08	0.000008	5.48241E-09	2.74121E-12	0.0000075	2.20893E-16	12409.63997	2.19296E-06
24	clip-plane-400.5-kls-8	3.01E-08	0.000009	1.50621E-08	7.53107E-12	0.0000085	3.21555E-16	23420.78168	5.31605E-06
25	clip-plane-400.5-kls-9	4.35E-08	0.00001	4.08351E-08	2.04176E-11	0.0000095	4.48921E-16	45481.46273	1.28953E-05
26	clip-plane-400.5-kls-10	7.88E-08	0.000011	1.39863E-07	6.99315E-11	0.0000105	6.06131E-16	115373.503	3.99608E-05

Figure 0.10 Example of eddy calculations in Excel